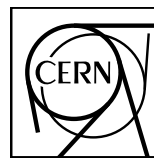


# EUROPEAN ORGANIZATION FOR NUCLEAR RESEARCH



Apparatus for Meson and Baryon  
Experimental Research



CERN-SPSC-2024-0XX

SPSC-SR-XXX

August XX, 2024

## AMBER Status Report 2024

The AMBER Collaboration

### Abstract

The report reviews the activities and the achievements of the Collaboration towards the current date. Covered items are the first completed data taking for antiproton production cross-section measurements, ongoing analysis and plans for 2025 running time; collected data so far and the preparations for the future runs for the measurements of the Proton Charge-Radius; preparations for the meson structure measurements by using Drell-Yan process, first results of Cherenkov detectors (CEDARs) test with high hadron beam intensity.



**Contents**

<b>1</b>	<b>Introduction</b>	<b>3</b>
<b>2</b>	<b>Antiproton Production Cross-Section Measurements</b>	<b>3</b>
2.1	Introduction . . . . .	3
2.2	Preliminary analysis of 2023 p-He data . . . . .	3
2.2.1	Status of the analysis of the antiproton-production in proton-helium collisions at $\sqrt{s_{NN}} = 18.9 \text{ GeV}/c$ . . . . .	3
2.3	Preparation to 2024 antiproton cross section run . . . . .	7
2.3.1	Motivation for an antiproton-production measurement in proton-proton and proton-deuterium collisions at AMBER . . . . .	7
2.3.2	Setup for the experiment . . . . .	9
2.3.3	Beam time and collected data . . . . .	9
2.3.4	Data Quality . . . . .	10
<b>3</b>	<b>Conclusion</b>	<b>10</b>
<b>4</b>	<b>Proton Charge-Radius Measurement</b>	<b>11</b>
4.1	Results from the 2021 Pilot Run . . . . .	12
4.2	Results from the 2023 Test Run . . . . .	12
4.2.1	Results of FriDAQ Test . . . . .	13
4.2.2	Results of TPC Test . . . . .	14
4.3	Plans for 2024/2025 . . . . .	15
<b>5</b>	<b>Meson structure measurement by using Drell-Yan process</b>	<b>16</b>
5.1	First results of the Cherenkov detectors (CEDAR's) 2023 test with high intensity hadron beam.	16
5.2	CEDAR detectors 2024 test with high intensity hadron beam. . . . .	17
5.3	Further future improvements to the M2 beamline . . . . .	17
<b>6</b>	<b>Hardware</b>	<b>19</b>
6.1	The Liquid Hydrogen/Deuterium target for APX . . . . .	19
6.2	CEDAR Detectors . . . . .	20
6.3	TPC and Gas System . . . . .	22
6.3.1	Beam test of the IKAR TPC in 2023 . . . . .	22
6.3.2	Preparation of the main TPC . . . . .	23
6.4	Unified Tracking Station UTS . . . . .	25
6.4.1	Scintillating Fiber Hodoscope (SFH) . . . . .	26

6.4.2	Silicon Pixel Detector (SPD) . . . . .	26
6.5	New Large Area Micromegas detectors . . . . .	28
6.6	GEM Detector Development . . . . .	30
6.6.1	New GEM detectors with triggered readout . . . . .	30
6.6.2	Triggerless GEM readout . . . . .	31
6.7	Vertex Detector for Drell-Yan . . . . .	33
6.8	FriDAQ . . . . .	35
6.9	Detector Control System . . . . .	36
<b>7</b>	<b>Publications, presentations to conferences and collaboration matters</b>	<b>38</b>
<b>8</b>	<b>References</b>	<b>39</b>

## 1 Introduction

The report describes first results of the antiproton production cross-sections measurement, and the status of the preparations for the proton charge-radius measurement and the meson structure measurement via Drell-Yan process, as well as the respective developments in hardware and organisation. The different physics cases are split into separate sections. Additional hardware-related information can be found in the dedicated hardware part of the document. This document is takes into account information presented in the previous SPSC reports of 2022 [1] and 2023 [2]. The given information covers the time between the release of the last report and the date of this report.

## 2 Antiproton Production Cross-Section Measurements

### 2.1 Introduction

In this section, we present an update about the data analysis of the p-He data collected in 2023 and a report about the preparation and execution of the 2024 data-taking with targets of liquid hydrogen and liquid deuterium.

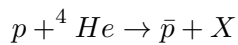
### 2.2 Preliminary analysis of 2023 p-He data

As discussed in our previous annual report, in 2023 we collected proton on liquid Helium target scattering data for several impinging proton momenta (60, 80, 100, 160, 190, 250 GeV/c). The data analysis was started from the 190 GeV/c AMBER proton run as this energy represents a benchmark that allows us to compare the detector performance with data collected by COMPASS in the previous years. This beam momentum corresponds to  $\sqrt{s_{NN}} = 18.9$  GeV/c in the center of mass frame of reference.

Despite technical difficulties related to the adoption of the event reconstruction framework due to the upgrade of the central CERN computing infrastructure LINUX version (RHEL9/Alma9), significant progress in the data analysis has been achieved and the first results were released for presentations at conferences, most significantly at the ICHEP 2024 conference. The current status and next steps are summarized below.

#### 2.2.1 Status of the analysis of the antiproton-production in proton-helium collisions at $\sqrt{s_{NN}} = 18.9$ GeV/c

Antiproton production cross-section data were collected in the period April-June 2023, including one month of detector commissioning. We are interested in the process:



To accurately measure this reaction, we first need to identify protons in the M2 secondary beam line. We used two Ring Imaging Cherenkov detectors (CEDARs) placed along the beam line upstream to the AMBER experiment, to inclusively identify the events with antiprotons in the final state. The charged particles produced in the proton interactions were registered as tracks in the AMBER spectrometer and their identification was performed using the AMBER RICH-1 detector. The accurate measurement of the double differential cross-section of the anti-proton production in the plane momentum-polar angle is one of the final goals of the experiment.

The physics data taking started on 19th May 2023. In about 2 months we collected a considerable data sample at six different beam momenta. A summary of the collected statistics in units of number of spills is shown in Tab. 1. The data analysis efforts have been focused on the period W01 (190 GeV/c), which will serve as a basis for the analysis of the other collected data.

To obtain a high track reconstruction efficiency and a good momentum measurement it is mandatory to perform the alignment of the spectrometer. The alignment procedure in AMBER follows the principles developed in COMPASS and aims to find the true position of tracking detectors starting from their approximate location established with a survey campaign performed before data taking. Although the whole iterative procedure is quite complex and requires several steps to be completed, is quite robust and it produced a satisfactory result.

The operation performance of the spectrometer is monitored during the whole period of data taking. In general, the stability of the detectors is ensured by proper commissioning and maintenance, but failures and errors may

Period name	Beam mom. [GeV/c]	Collision energy $\sqrt{s_{NN}}$ [GeV]	Start Date	End Date	# of spills
W01	190	18.9	19.05	24.05	11000
W02-W03	60	10.7	24.05	30.05	37000
W04	100	13.8	01.06	11.06	13700
W05	250	21.7	11.06	14.06	7300
W06	160	17.3	14.06	17.06	8500
W07	80	12.3	17.06	25.06	13400

Table 1: Summary of the data taking periods, with the collected statistic in units of number of spills.

influence a single detector or the whole apparatus. For this reason, a stability analysis has been performed to define the data sample collected in stable conditions. The data analysis has been limited to this sample. The selected data conditions are based on:

1. online monitoring during data taking
2. spill by spill analysis
3. run stability study

Online monitoring allows us to identify channel-by-channel possible problems with detectors. This is usually done directly during data taking, but the results can be used as well for later stages to identify possible sources of instabilities. Then a rejection based on macro/tracking variables is performed at the spill level. The spill analysis showed a spill rejection rate of 10% in the data taking period W01. Eventually one can analyze whole runs to check the stability of physics variables, like mass and width of  $K_S^0$  and  $\Lambda/\bar{\Lambda}$ . The run stability studies showed that no full runs were rejected.

The determination of the target position and dimension was carried out using the reconstruction of the tracks with the beam tracker (upstream of the target) and the proper spectrometer (downstream of the target) this allowed the identification of the interaction vertexes of the proton beam with AMBER. Only events where the primary vertexes are inside the target volume are selected for the analysis. To minimize the systematic error induced by interactions with other target materials (e.g. the general support structure of the target), the exact dimension of the main Helium Target volume has to be determined. Furthermore, the correct target position is needed for the precise estimation of the incoming proton flux to derive the luminosity. Finally the most precise as possible target geometry has to be implemented in the Monte Carlo for applying proper corrections. The target region along Z is identified by looking at the Z distribution of primary vertices. The nominal length of the target is 140 cm, from -70 cm to 70 cm. Fig. 1 shows the vertexes distribution, the target region is clearly visible within the range of the nominal coordinates. On the XY plane, perpendicular to the Z axis, the vertex distribution shows a ring with a radius of  $\sim 3.6$  cm. The X and Y coordinates of the target center were studied as a function of Z. In general, we observe a tilt in X of less than 1 mm and in Y of about 1.2 mm over the 1.40 m target length. The value of the radius is quite stable, with minor dependence on Z ( $< 0.5$  mm).

As previously discussed, the identification of the incoming beam particle is performed by using the CEDARs detectors installed upstream of the target. In 2023 we set the pressures of both CEDARs in such a way to positively tag the protons in the beam. At 190 GeV/c, the protons signal is very well separated from the one of pion and kaons and we can obtain an almost pure sample of protons. The tagging efficiency with a 6-fold (over 8) requirement on both CEDARs was evaluated from the online monitoring and confirmed with the data sample, with an efficiency of 96%. The misidentification probability was extracted from dedicated runs in which one CEDAR is set on pion and the other on proton. The resulting misidentification probability is  $\sim 10^{-4}$ . Considering that the pion fraction in the beam at this energy is  $\sim 25\%$ , a dual CEDARs proton signal provides a high-purity proton sample. In Fig. 2 the many-fold occurrences are also shown. It is clearly visible that the proton tagging is efficient with 7-8 fold in CE2 and 6-8 in CE1, while the  $\sim 21\%$  multiplicity at 0 fold in CE1 and CE2 is due to the positive hadron beam composition at 190 GeV/c, which is made of  $\sim 75\%$  protons and remaining 25% of pions and a small fraction of kaons.

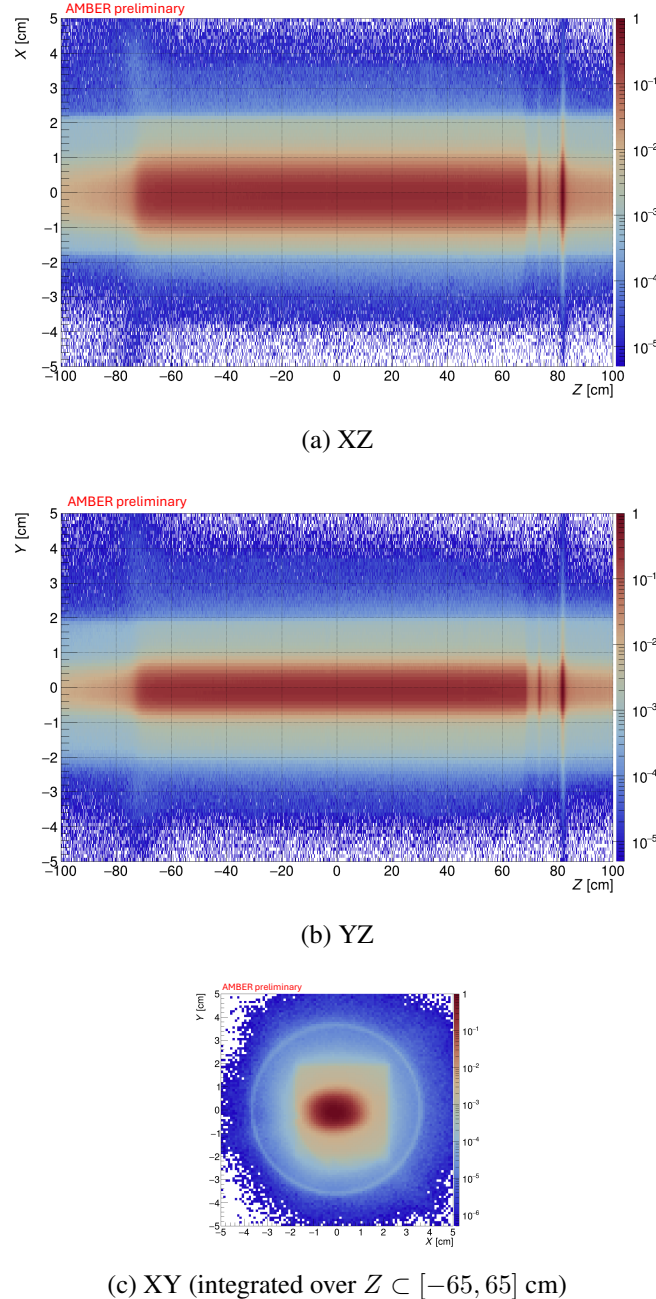


Fig. 1: Distribution of the primary vertices in the target region in the different projections. The plot is arbitrarily normalized. The mixing chamber circumference is clearly visible in the X-Y coordinates plane with a radius of  $\sim 3.6$  cm. Also, the sub-structure of the  $2 \times 2$  cm $^2$  fiber detector is visible. The liquid helium target is visible from  $Z = -70$  cm to  $Z = +70$  cm. Reduced sample.

The RICH-1 is used for the identification of the final state hadrons. The identification and misidentification probabilities of the RICH-1 have been estimated from the data using a track sample extracted from the decays of the so-called V0 secondary vertices, i.e. the decays of the neutral  $\Lambda, \bar{\Lambda}, K_S^0, \phi$  (also listed in Tab. 2).

The so-called Armenteros-Podolanski plot is produced by plotting the  $p_T$  of one of the two produced particles, versus the asymmetry of the laboratory longitudinal momenta of the two particles ( $\alpha$ ). In this representation, the V0s population appears as typical arc shapes visible in Fig. 3.

$$\alpha = \frac{p_l^+ - p_l^-}{p_l^+ + p_l^-} \quad (1)$$

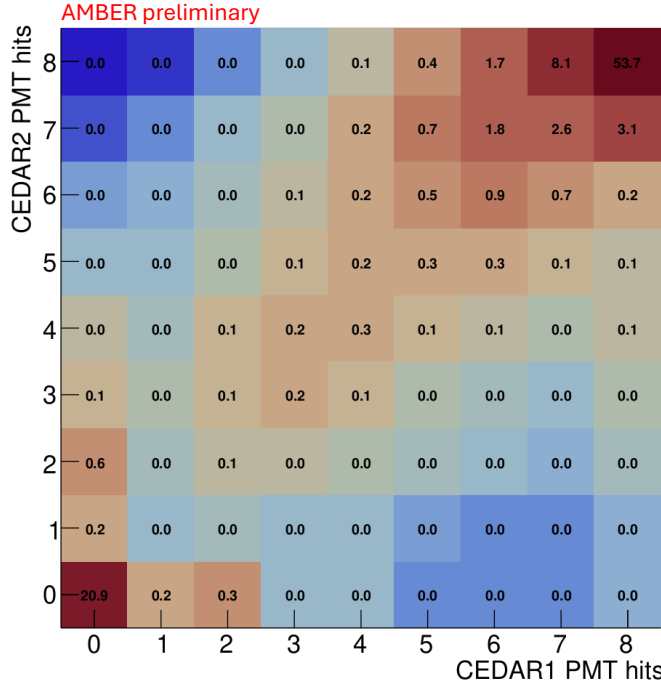


Fig. 2: Many-fold occurrences in percentage from 1 to 100 %, normalized on the number of events.

Hadrons	Decays	
	Channel	BR
$K_S$	$\pi^+ \pi^-$	$(69.20 \pm 0.05)\%$
$\phi$	$K^+ K^-$	$(48.9 \pm 0.5)\%$
$\Lambda(\bar{\Lambda})$	$p\pi^- (\bar{p}\pi^+)$	$(63.9 \pm 0.5)\%$

Table 2: Summary of the  $V_0$ s decay channels.

$$p_l = p \cos \theta \quad (2)$$

$$p_T = p \sin \theta \quad (3)$$

The efficiencies and misidentification probabilities are then collected into a PID matrix, used in the matrix formalism for the unfolding of the true number of identified hadrons as a function of momentum and  $p_T$  in the laboratory frame. The true number  $N_{true}^h = \frac{N_{id}^h}{\varepsilon}$  of a certain hadron species  $h = \pi, K, p$  in the AMBER apparatus is obtained from the identified number of hadrons  $N_{id}^h = N_{measured}^h \cdot \frac{\gamma}{\epsilon_{RICH}}$  and  $\varepsilon = A \cdot \epsilon_{DAQ} \cdot \epsilon_{VETO}$ . The  $\varepsilon$  term includes the acceptance  $A = \epsilon_{geom} \cdot \epsilon_{tracking}$  and the lifetime correction of DAQ and VETO. The number of identified hadrons accounts for the purity  $\gamma$  of the measured  $h$  sample and for the efficiency of the RICH in identifying that species  $\epsilon_{RICH}$ . The measured number of hadrons  $N_{measured}^h$  is computed after a selection of inelastic events in the helium target induced by protons in the beam. From these events, the track selection follows minimum criteria to ensure a good reconstruction of the hadron candidates. The bin size of the phase space was optimized with a dedicated study with a reconstructed MC sample. The statistical uncertainty on the true number of antiprotons is shown in Fig. 4. This result shows the excellent coverage of the phase space in terms of collected statistics by AMBER. We expect that the systematic uncertainty on the RICH-1 PID matrix extraction and the luminosity determination will be the dominant contributors to the total error. The analysis of the other proton beam momenta is ongoing and results will be soon available.

The preliminary results on the 2023 p-He data collected at  $\sqrt{s_{NN}} = 18.9 \text{ GeV}/c$  have been released by the AMBER Collaboration and presented at ICHEP Conference in July 2024.

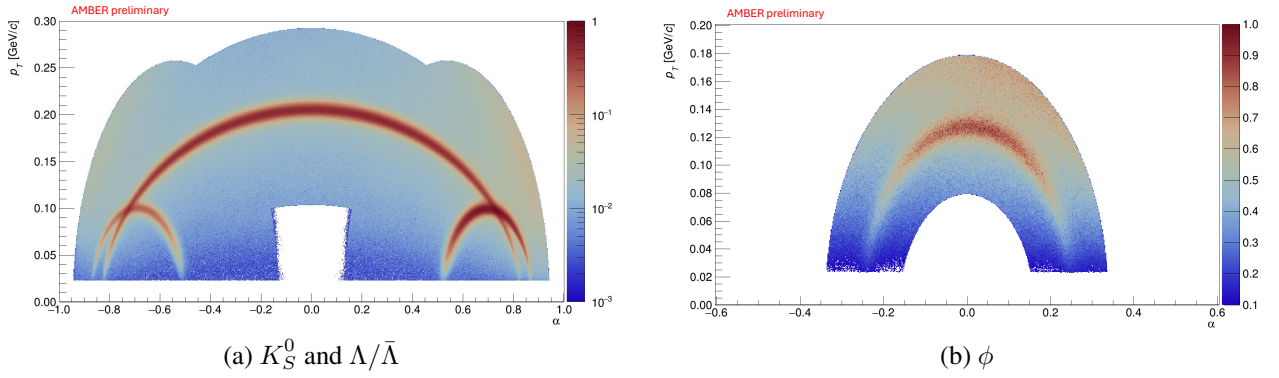


Fig. 3: Armenteros-Podolanski plot for the selected two body decays. On the left, the main arc is the population of  $K_S^0$  candidates, with the two smaller arcs for  $\Lambda$  and  $\bar{\Lambda}$ . On the right, the  $\phi$  arc is visible.

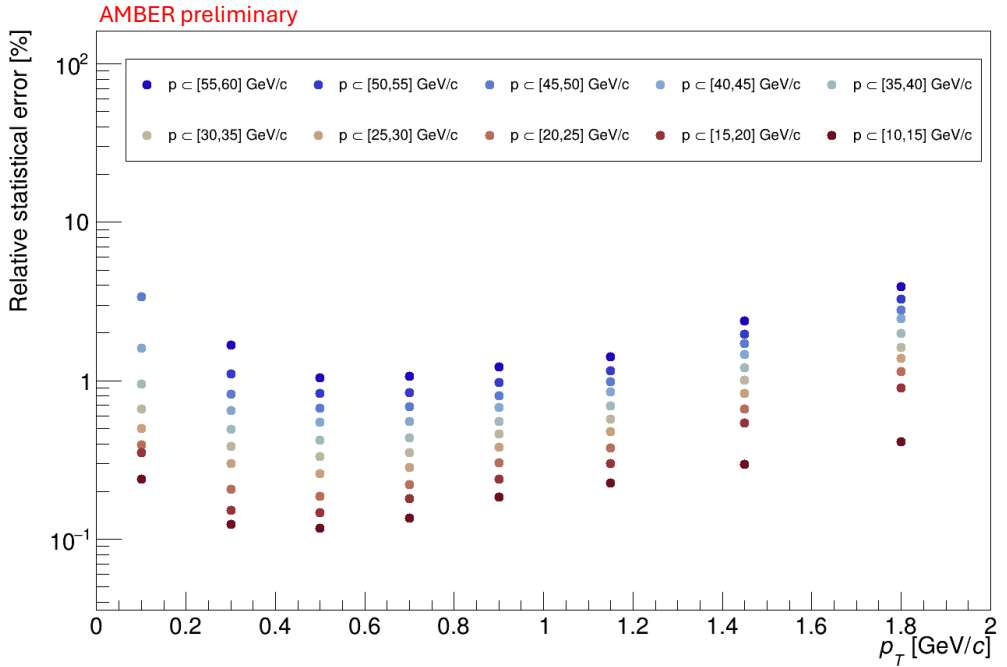


Fig. 4: Statistical error on the RICH-unfolded number of antiprotons in the different bins of the phase space calculated as the square root of the number of entries. The data points are located in the average of the bin limits.

## 2.3 Preparation to 2024 antiproton cross section run

In parallel to the data analysis of the 2023 data on antiproton-production in proton-helium collisions, we performed a measurement of the antiproton-production in proton-proton and proton-deuterium collisions this year (2024). In the following, we will briefly summarize the motivation and setup for this measurement and give an overview of the already finished data taking period.

### 2.3.1 Motivation for an antiproton-production measurement in proton-proton and proton-deuterium collisions at AMBER

Although already results are available on  $p + p \rightarrow \bar{p} + X$ , the most recent ones from the NA61 collaboration at 20, 31, 40, 80, and 158 GeV/c [3], performing a new measurement on  $p + p \rightarrow \bar{p} + X$  having a large overlap with the already available data sets would allow for a direct comparison of the results and important studies of possible systematic effects, which are of special interest to verify the unique  $p + He$  dataset taken last year. In

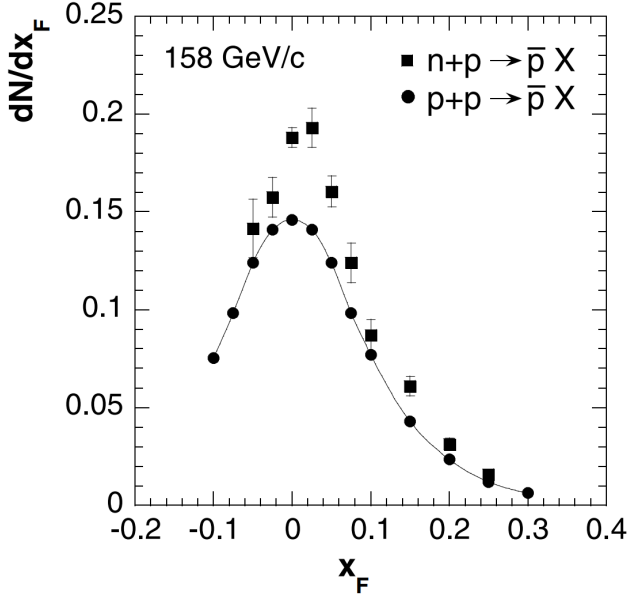


Fig. 5: Experimental data of antiproton production in  $n + p$  and  $p + p$  collisions from NA49. Figure taken from [4].

addition, the AMBER data will also extend the range of measured collision energies by a measurement using a 250 GeV/c proton beam and increase the phase-space coverage of antiprotons with respect to NA61, especially for large transverse momenta.

Besides the production of antiprotons via direct hadronization or from the decay of antihyperons produced in the collisions—which both can be probed directly by accelerator-based experiments—the contribution from antineutrons is experimentally completely unexplored. Most often the antineutron yield from collisions is only modeled from the underlying physical principles based on isospin symmetry. The production rate of  $\bar{p} - p$  and  $\bar{n} - n$  pairs is then expected to be equal. Additionally, antinucleons can also be created in pairs of  $\bar{p} - n$  or  $\bar{n} - p$ , and their production rate is also expected to be equal. However, measurements of NA49 at  $\sqrt{s} = 17.3$  GeV gave hints that the production of the mixed antinucleon-nucleon pairs might depend on the value of  $I_3$ , the third component of the isospin, of the initial state—or equally the charge value of the initial state [4]. For  $p + p$  collisions, NA49 measured an enhancement of  $\bar{n} - p$  pairs and a depletion of  $\bar{p} - n$  pairs relative to  $n + p$  collisions. For cosmic-ray interactions in the Galaxy, the underlying nucleon-nucleon interactions feature more often  $p + p$  collisions than  $n + p$  or  $n + n$  collisions, resulting potentially in an enhanced production of antineutrons over antiprotons. The strength of this asymmetry, its dependence on the collision energy, and the distribution of the asymmetry within the phase space of the produced antiparticles in the collision are not yet well known, due to the lack of experimental data. The only existing experimental data on this effect from NA49 shows that the asymmetry of the production might reach 50% to 60% and is maximal at  $x_F = 0$ . A confirmation of this asymmetry and a more detailed study of its phase-space and collision-energy dependence, however, is pending.

M. Winkler performed a first estimate of the collision-energy dependence of the effect by interpolating the available data [5]. In Figure 6, the energy-dependent isospin enhancement factor is shown, which is defined as  $\Delta_{is} = f_{\bar{n}}^0/f_{\bar{p}}^0 - 1$ , with  $f_{\bar{n}}^0$  and  $f_{\bar{p}}^0$  being the prompt-production cross-section of antineutrons and antiprotons.

The isospin asymmetry affects mainly the production of antiparticles at lower collision energies but its existence and magnitude are experimentally not yet clarified. The possible isospin asymmetry in the production of antiprotons and antineutrons poses one of the dominating uncertainties in the modeling of antiprotons produced in cosmic collisions.

To verify or exclude such an isospin-asymmetric production of antiprotons and antineutrons, AMBER plans to measure the antiproton production successively in  $p + p$  and  $p + D$  collisions, with a nearly identical setup. By replacing the liquid hydrogen in the target with liquid deuterium, AMBER can indirectly measure the antiproton-production cross section in  $p + n$  collisions by subtracting the measured  $p + p \rightarrow \bar{p} + X$  cross section from the

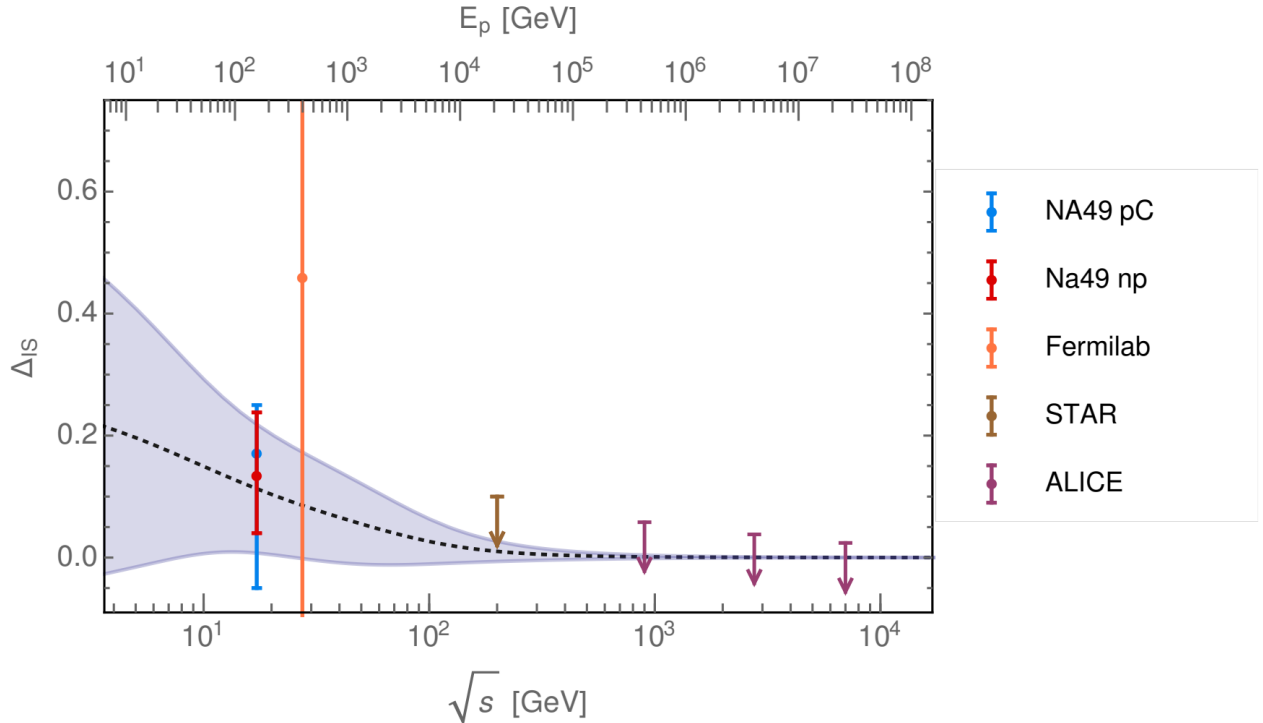


Fig. 6: Estimation of the isospin asymmetry of antineutron and antiproton production as a function of collision energy by M. Winkler using existing experimental data. Figure taken from Winkler [5].

measured  $p + D \rightarrow \bar{p} + X$  cross section with minimal systematic uncertainty due to the identical experimental setup. Performing these measurements at several different collision energies would allow to constrain a possible isospin-asymmetric production of antiprotons and antineutrons and the dependence on the collision energy. By this, the modeling uncertainties of galactic antiproton production can be further reduced [6]. By providing three measurements of the isospin asymmetry at different beam energies, e.g. 80 GeV/c, 160 GeV/c, and 250 GeV/c, with measurement uncertainties of the individual data point of around 5%, AMBER would constrain the level of the isospin asymmetric production of antiprotons below roughly 10% and constrain the collision-energy dependence of this effect. In Figure 7, the impact of the additional measurements by AMBER on the uncertainty of the isospin factor is projected.

### 2.3.2 Setup for the experiment

The setup of the spectrometer is identical to the 2023 measurement using the liquid helium target except for the cryogenic target. The setup of the liquid hydrogen and deuterium target is described in Section 6.1.

### 2.3.3 Beam time and collected data

The beam time for the measurement of antiproton production in proton-proton and proton-deuterium was scheduled for 10.04.2024 until 19.06.2024. However, due to increased safety constraints for the liquid hydrogen target which led to a delay in the start of physics-data taking (09.06), the beam time was prolonged until 17.07. In Table 3, the different measurements taken during the physics beam time are chronologically listed. For each setting, additionally trigger-efficiency runs and alignment runs (using a muon beam) have been recorded. During the switchover of the target between 30.06 and 02.07 and after the completion of the physics runs on 15.07, empty-target measurements with the different beam settings were performed to study the background from interactions outside of the hydrogen/ deuterium.

An overview of the course of the number of recorded spills is given in Figure 8.

Especially during the begin of the physics-data taking, several issues at the accelerator complex and the recovery of the beam after the technical stop delayed the progress of the data taking further. In order to compensate for

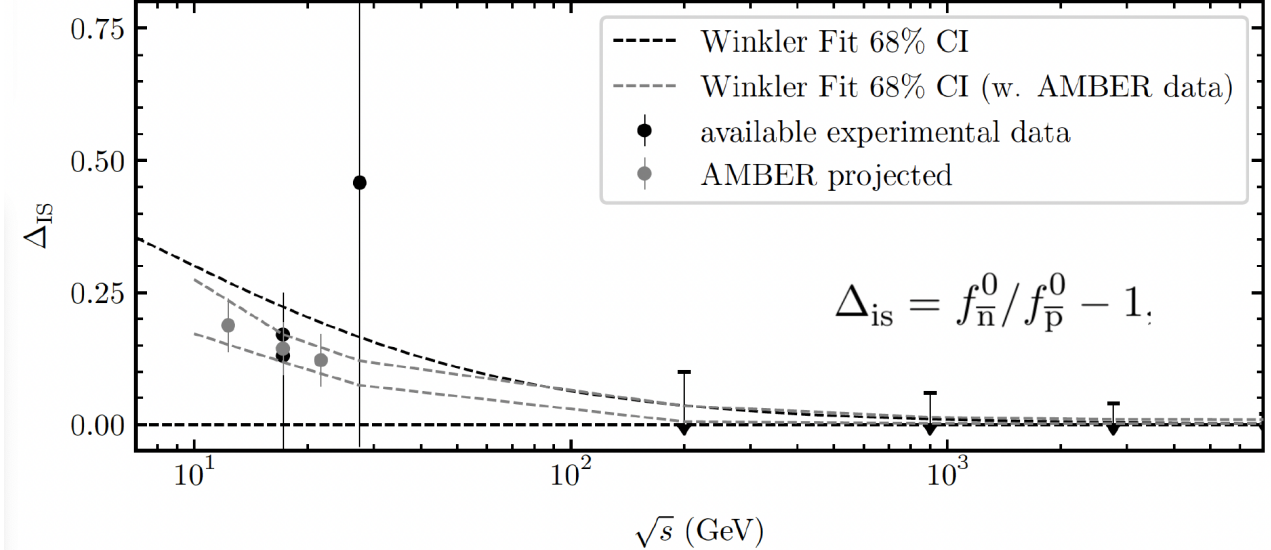


Fig. 7: Estimation of the impact of the AMBER measurement of the isospin factor using experimental data at 3 different collision energies.

Table 3: Conducted measurements during the 2024 physics run.

Beam momentum (GeV/c)	Collision energy ( $\sqrt{s_{NN}}$ ) (GeV)	Target	Start Date	End Date	Number of spills
250	21.7	Hydrogen	09.06	19.06	8600
80	12.3	Hydrogen	20.06	25.06	16500
160	17.3	Hydrogen	25.06	30.06	12500
160	17.3	Deuterium	02.07	05.07	13000
80	12.3	Deuterium	06.07	11.07	16500
250	21.7	Deuterium	11.07	15.07	9100

this, AMBER decided to postpone the high-intensity DY test that was planned for the last 5 days of the data-taking period to the October beam time in order to provide a successful antiproton-production-measurement data taking with the required statistics to perform the planned analyses.

### 2.3.4 Data Quality

To guarantee the best data quality, an online-reconstruction chain was set up during the data taking, and first alignment analyses were performed to check that the different beam settings used were correct and the liquid hydrogen/deuterium target was illuminated centrally by the beam. In Figure 9, we show exemplary for 250 GeV/c and the hydrogen target the distribution of reconstructed vertices (with at least 3 outgoing tracks) along the beam direction (Figure 9(a)) and in perpendicular plane within the target-cell region (Figure 9(b))). One can notice, that the beam was well centered in the target cell that had a diameter of only 4 cm.

## 3 Conclusion

Despite delays related to the increased safety constraints and issues of beam delivery especially in the first week after the start of the physics data taking, the beam time can be regarded as a success. Measurements with proposed energy and target settings that have been proposed for the measurement to the SPSC in November 2023 have been performed and the proposed statistics for all of the datasets have been reached. The data analysis

### AMBER antiproton-measurement data-taking

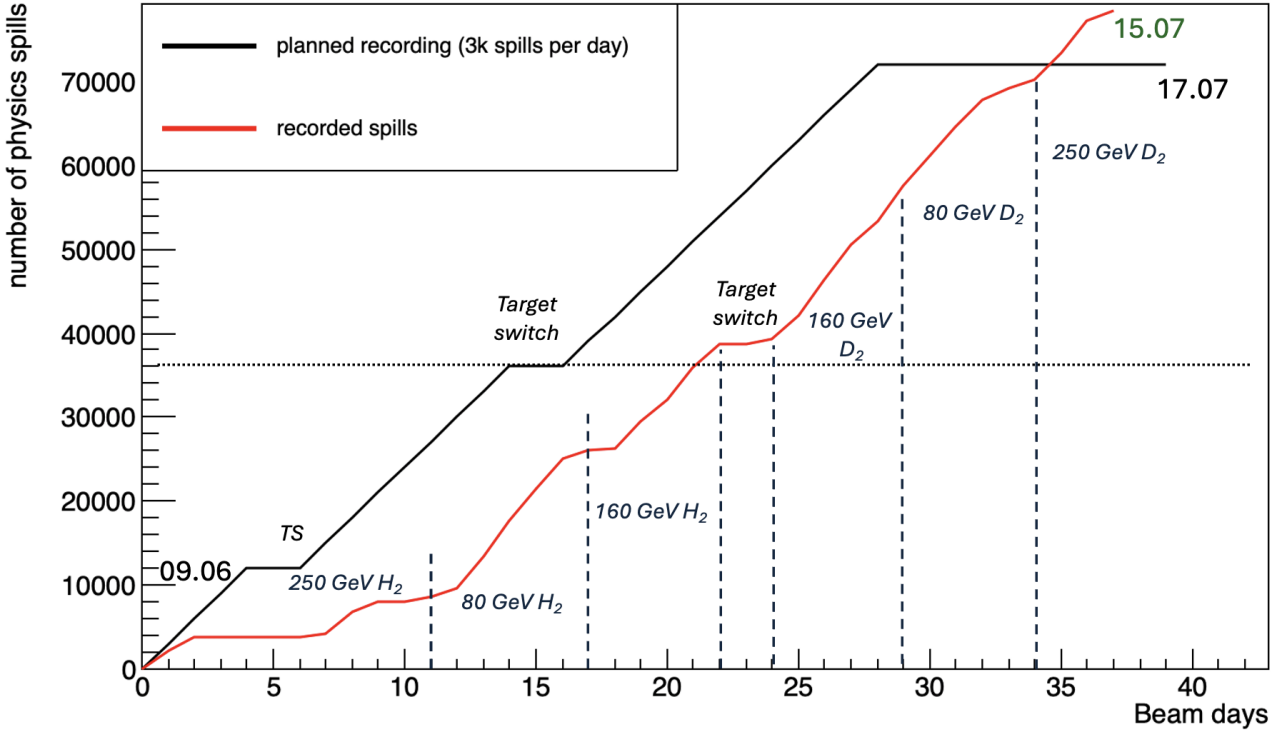


Fig. 8: Spill count of the AMBER physics data taking as a function of beam days.

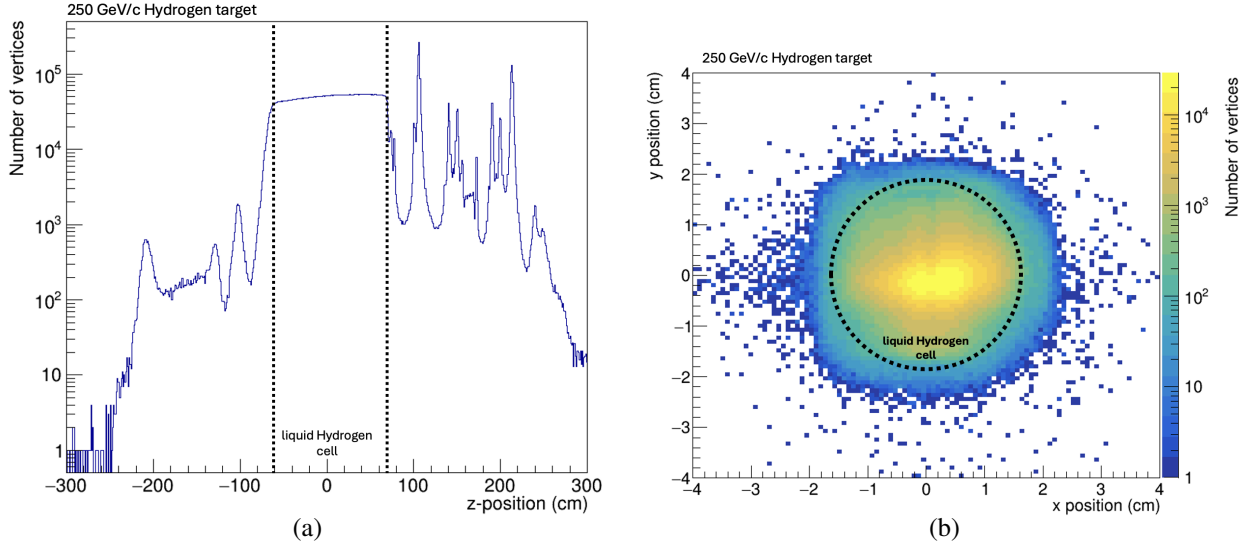


Fig. 9: Distribution of reconstructed vertices in one run of the dataset with 250 GeV/c beam and hydrogen target. In (a) the vertex distribution along the beam is shown; In (b), the vertex distribution in the horizontal and vertical direction within the target region ( $-70\text{ cm} < z < 70\text{ cm}$ ) is shown.

of the 2024 data will go in parallel to the ongoing data analysis of 2023 data and complete the measurements of antiproton-production cross sections in AMBER.

#### 4 Proton Charge-Radius Measurement

We present an update with respect to the previous report [2] from 2023. A more detailed analysis of our combined data taking during the Pilot Run 2021 is shown (cf. Sec. 4.1). Another Test Run was conducted in

2023, focusing on studies of individual detectors and the common readout. First results of this run are presented (cf. Sec. 4.2). The plans for another Test Run in 2024 and a Physics Run in 2025 are described (cf. Sec. 4.3).

#### 4.1 Results from the 2021 Pilot Run

In both previous SPSC reports [1][2], preliminary results of the Pilot Run in 2021 at the M2 test beam location were presented. The setup consisted of an IKAR TPC, which is a smaller version of the final TPC with an operational pressure of up to 8 bar. Surrounding this TPC, a close-to-final layout of the surrounding tracker system consisting of four stations of silicon-microstrip detectors and two scintillating fiber hodoscopes was used. The TPC and the tracking system were read out with separate data acquisitions (DAQ).

During the data taking, we have injected a generated signal to determine the noise level of the TPC continuously. In a dedicated intensity scan, we have measured the noise level for different intensities at two pressure settings, see Figure 10. We see that the noise at these pressures and an intensity of 2 MHz is mostly dominated by electronic noise and below 25 keV for the central pads.

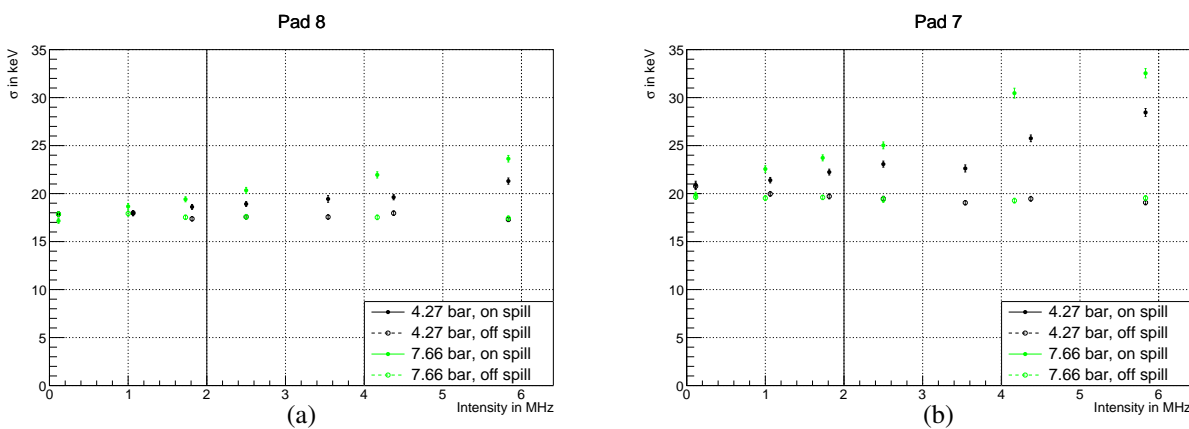


Fig. 10: The beam and electronic noise of single pads of the TPC for different beam intensities at two pressure settings during the Pilot Run 2021. The resolutions are shown for a central pad in (a) and for a pad on the first ring in (b). [7]

The data from both detector systems was combined using a common trigger logic (TRLO) timestamp. The resulting time difference plot and more correlations are visible in Figure 11. There is a clear correlation time peak shown in Figure 11(a). We have selected about 2000 correlated events. The combinatorial background was reduced by a selection of the drift cell using kinematic variables. Due to the finite drift velocity of electrons in the TPC, this time difference depends on the  $z$ -position of the scattering vertex. The extracted drift velocity from a linear fit (cf. Figure 11(b)) is in agreement with expectations. The energy and azimuthal angle of the recoil proton can be extracted from the TPC measurement and the tracking detectors and are in good agreement (cf. Figures 11(c), 11(d)).

#### 4.2 Results from the 2023 Test Run

We had a Test Run in September 2023, which was dedicated to detector and DAQ tests. One important step for the main measurement is the integration of all detectors into the new trigger-less FriDAQ. Several detectors were integrated in 2023, see section 4.2.1. Results of the TPC test are summarized in section 4.2.2. During the run, the UTS detector vessels were installed and commissioned and detector tests with an SFH prototype were performed, as described in Sec. 6.4. Gas Electron Multiplier (GEM) detectors play a large role in our expected spectrometer. These detectors were read out with a VMM chip and results are described in section 6.6.2.

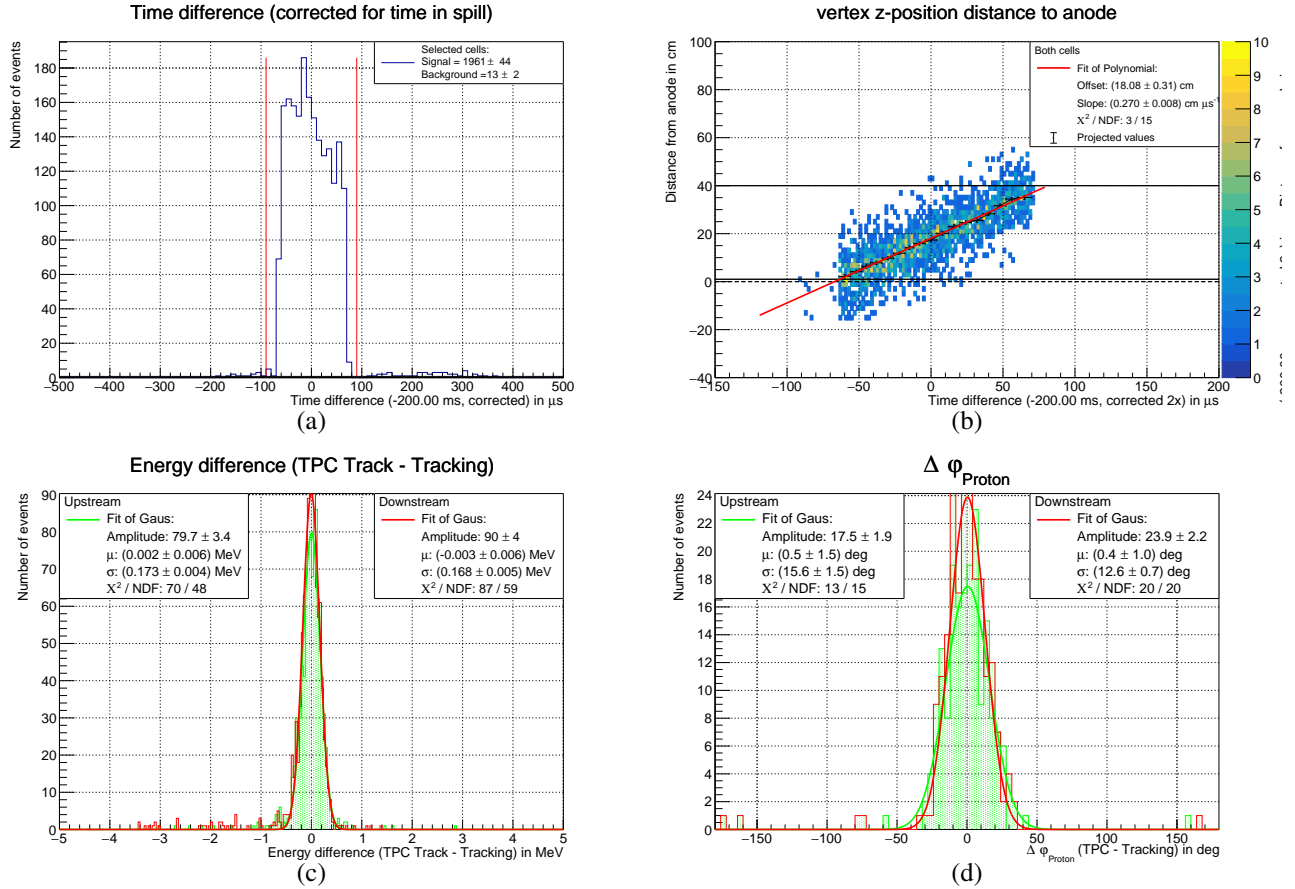


Fig. 11: Results of the combined data taking during the Pilot Run 2021. The TRLO time stamp difference between the tracking and TPC system is shown in (a). We see a clear time difference peak. The drift velocity is extracted in (b). The resulting correlations of energy and azimuthal angle are shown in (c) and (d). [7]

#### 4.2.1 Results of FriDAQ Test

In 2023 the FriDAQ setup included 6 DHMUX modules, Time Slice Builder, two read out servers equipped with external disk storage of 0.5 PByte each, high performance network switch, and 100 Gbps Ethernet link to CERN computing center.

The Time Slice Builder and DAQ software were extensively tested with software and hardware generated data. The generated data were transferred from the Readout Engine computers through HLT to CTI. During the PRM run the DAQ was used for commissioning of front-end electronics. Few software bugs were identified and removed.

For the 2023 PRM run we successfully integrated front-end electronics of TPC, SPD, and Hodoscope detectors.

The TPC readout is based on commercial flash ADC modules SIS3316, which do not support streaming readout mode. For integration of them into streaming DAQ, we worked out a scheme where the TPC readout works in self triggering mode synchronously with the streaming DAQ. TCS(Time Control System) provided common 38.88 MHz and initiates the TPC readout by a coincidence of recoil proton trigger with Time Slice signal. The digitized data were transmitted from each ADC module directly to the TPC server together with the Time Tag via multiple Gigabit Ethernet interfaces. During the test a synchronous acquisition of the TPC readout system with the streaming DAQ was successfully demonstrated.

The Silicon Pixel detectors will be readout by a newly developed CMAD front-end card. In 2023 we integrated the CMAD card in FriDAQ without ALPIDE detector.

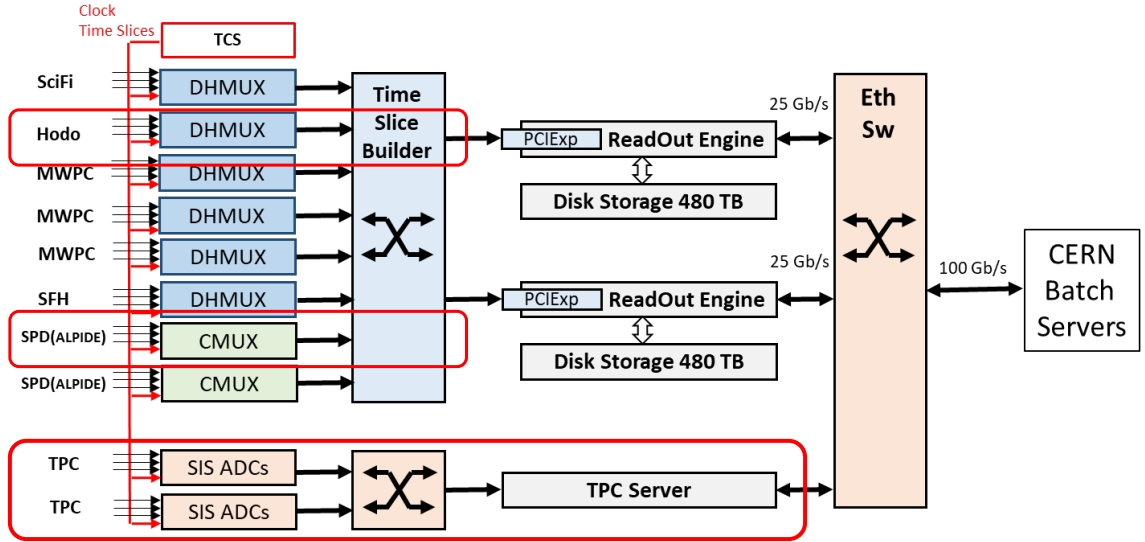


Fig. 12: The FriDAQ architecture during the 2023 PRM run.

The Hodoscope detectors were equipped with iFTDC cards that were already commissioned and widely used for data taking by AMBER. During the run we verified and evaluated stability of the read out chain. Few problems were observed. First of all instability of start of the run procedure due to race conditions and a lack of error diagnostics. The DHMUX firmware has been revised and improved.

#### 4.2.2 Results of TPC Test

In 2023, an upgraded IKAR TPC was used. While the TPC used the same vessel as in 2021, new electronics as described in section 4.2.1 and control systems were used. The gas quality was improved using a purification unit, results can be seen in Figure 13. Due to attachment of drift electrons, measured energies are decreased proportional to impurities in the gas. We see that the purification unit successfully improves the gas quality, leading to an increase of the measured  $\alpha$ -energy, especially at higher drift distances. Further results are described in section 6.3.1.

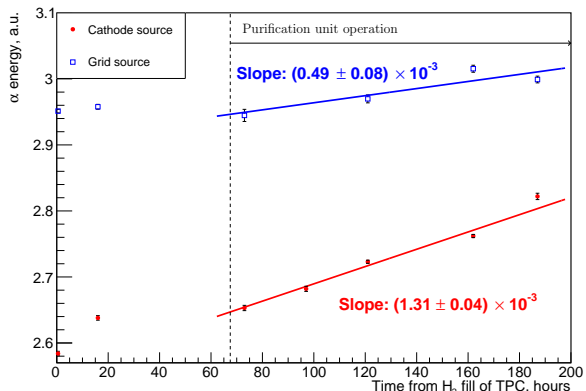


Fig. 13: The mean energies of  $\alpha$ -sources at the grid and the cathode with time. We see an increase of the energies with time, which can be attributed to an improvement of the gas quality. Initially, we see a "self-cleaning" effect of the TPC vessel and later the effect of the purification unit. [8]

### 4.3 Plans for 2024/2025

The main components of the new setup for the proton radius measurements are intensively worked on, but are delayed as compared to the original planning in 2021. The new TPC will have to be completed without participation of Russian institutions after November 2024. Therefore the main focus in autumn 2024 is to profit from the Russian expertise as long as it can be provided, remote and in presence at CERN. The respective progress is described in section 6.3.2. We are determined to have first successful tests in 2024, and will have the new TPC operational for a physics run in 2025. If the developments this year go smoothly, this may be already in the beginning of the 2025 beam time, however due to the uncertainties in the needed restructuring of the project, additional delays may lead to a readiness only in the middle of next year. In any case, AMBER will greatly profit from possibilities to run a part of the program also in 2026.

At the same level, the unified tracking stations (cf. 6.4) are needed, including the silicon pixel detectors (SPD) with high spatial resolution and the scintillating fiber hodoscopes (SFH) with high time resolution. All detectors need to be included in the new FriDAQ streaming readout system (cf. 6.8), which made vast progress in the last year but especially the interfaces to the detectors still need substantial development work. Regarding SFH (cf. 6.4.1), the respective readout electronics is designed and it is planned to test a first detector module in the beam in autumn 2024.

The project for the ALPIDE detectors (cf. 6.4.2) suffered from several restructuring processes, that became necessary due to changes in the funding possibilities of the respective AMBER groups. The respective delay will allow the detectors to be available only at some point in 2025, however still in line with our expectations for the TPC.

We have acquired a list of necessary detectors in the envisaged final setup. These allow us to determine the relevant information of our muon kinematics. The relative resolution of the squared four-momentum transfer  $Q^2$  is shown in Figure 14(a) for both pressure settings. Additionally, we require the determination of the muon momentum using a spectrometer magnet (SM2) and a successful muon identification. We can determine the expected acceptance of all tracks, which fulfill the geometrical acceptance of our TPC beam windows, in Figure 14(b). This acceptance is close to 1 and is flat in the relevant  $Q^2$  range.

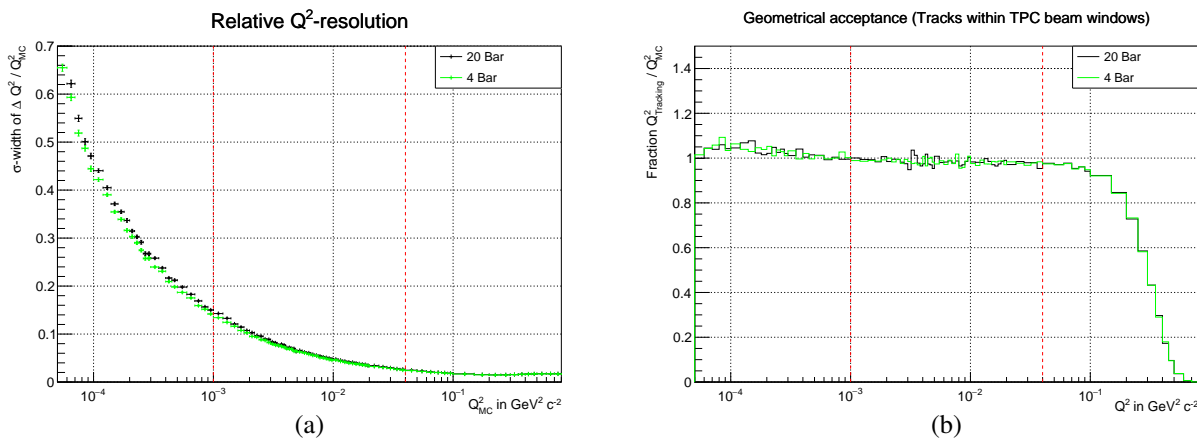


Fig. 14: The relative resolution of the squared four-momentum transfer  $Q^2$  is shown in (a). The acceptance from the reconstruction including momentum determination and muon identification is shown in (b). [7]

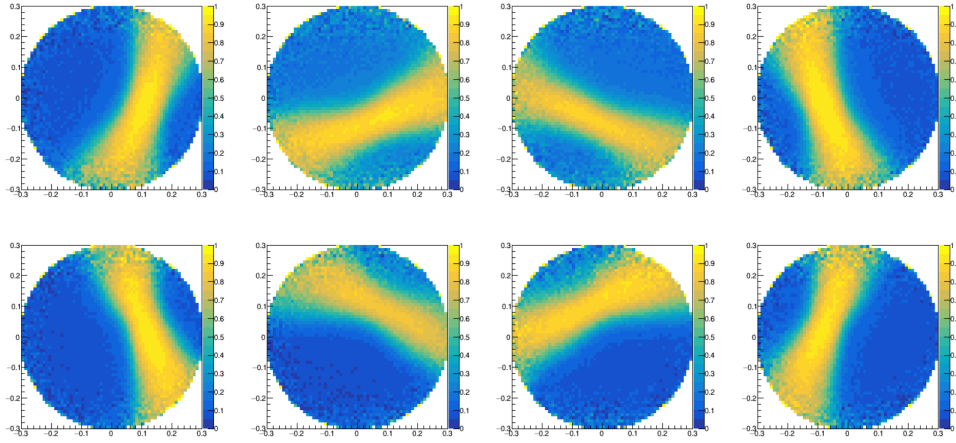


Fig. 15: Response of the CEDAR2 PMTs in bins of beam slope, with corrected beam transport matrix, and CEDAR tuned to kaon peak.

## 5 Meson structure measurement by using Drell-Yan process

### 5.1 First results of the Cherenkov detectors (CEDAR's) 2023 test with high intensity hadron beam.

As presented in the previous report [1], the CEDAR detectors are a crucial element of the Drell-Yan (DY) setup. These detectors located in the M2 beam line upstream from the target region of the spectrometer identify the beam particle. The positive (negative) hadron beam includes protons (antiprotons), pions and kaons [9], effective beam particle identification is therefore critical for any possible kaon-DY physics with either beam charges, and pion-DY with positive beam charge.

There are several challenges when operating the CEDAR detectors: the beam divergence at CEDAR location, the uncertainty on the reconstructed beam particle parameters, the high beam intensity required by the Drell-Yan measurement, the noise level seen by the CEDAR PMT induced mostly by the beam halo which produces Cherenkov radiation when hitting the PMTs windows. The beam trajectory, measured by the beam telescope detectors, is reconstructed and extrapolated to the upstream region, since there are no tracking detectors at the CEDARs location. This extrapolation is done using a beam transport matrix, obtained from dedicated simulations using the MADX package. Six transport matrices were prepared by the Beam group (BE/EA) reflecting the different optics used for the beam energies: 60, 80, 100, 160, 190 and 250 GeV.

In 2023 a test of CEDARs was performed, to address the challenging conditions of the CEDARs in Drell-Yan measurement conditions. The test took place immediately after the antiproton cross section measurement Run and lasted from 30 June to 4 July. It used two different beam energies, 190 GeV and 160 GeV, both beam charges, and several hadron beam intensities, from the one used at the APX test to the nominal for Drell-Yan measurements from the AMBER proposal,  $3.5 \times 10^8$  particles/spill. In order to improve the space resolution of the beam telescope the much more precise silicon tracking detectors (3 stations of 4 planes each) were added to the usual scintillating fiber detectors (7 tracking planes), in a setup similar to that of the antiproton Production Cross-Section Measurement (APX). The transport matrices from BE was further corrected using the tracking information from the scintillating fiber detectors to improve the extrapolation precision. With the updated transport matrices, we obtained the PMT response from CEDAR2 when the detector was tuned on the kaon peak, shown in Fig. 15. In this figure, the green color roughly corresponds to the kaon signal. Following a similar likelihood method developed during the COMPASS time [9], we obtain the likelihood distribution for kaon particles, with a selection of beam tracks extrapolated at the CEDAR position with polar angles below 100  $\mu\text{rad}$ , as shown in Fig. 16. For the first time, we are able to observe a clear kaon signal in the high intensity beam. Further optimization of the analysis method is still underway.

The goals of the 2023 CEDARs test were not fully achieved, due to CEDAR hardware limitations: the CEDAR positioning motors that could not be controlled with enough precision, and the control of the CEDARs diaphragm aperture that was not working properly. The CEDAR detectors were refurbished and commissioned again during the APX run in 2024, the details of the 2024 commissioning can be found in Sec. 6.2.

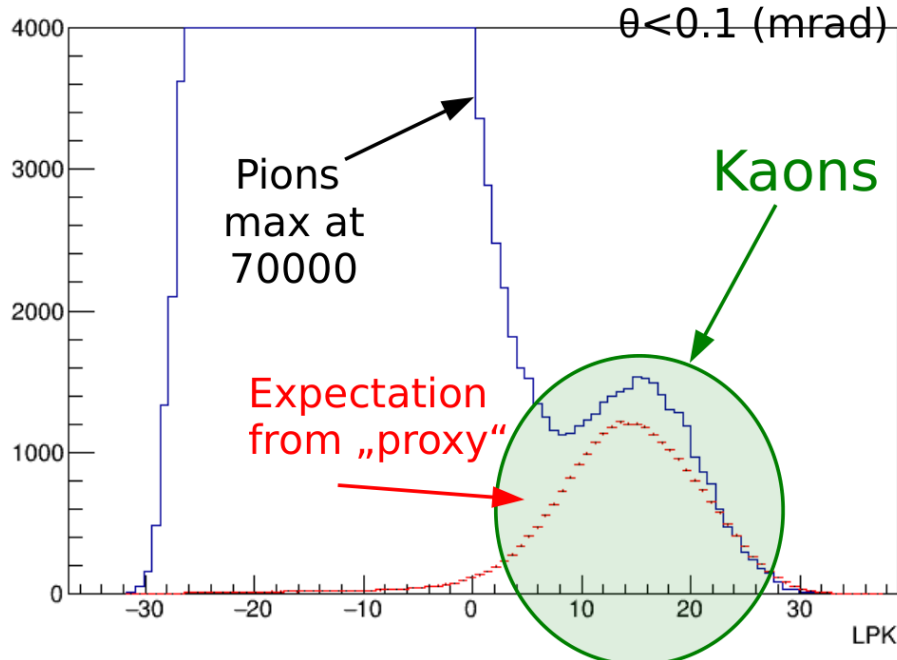


Fig. 16: Kaon likelihood distribution from the 2023 CEDAR test run.

## 5.2 CEDAR detectors 2024 test with high intensity hadron beam.

We plan to carry out another test of the CEDARs to optimize the kaon identification capability in the beginning of October. The test entails a systematic scan of beam intensity (from  $2 \times 10^6$  to  $360 \times 10^6$  particles per spill), energy (160 and 190 GeV), and CEDARs configurations, including an optimisation study varying the CEDARs diaphragm apertures. Additionally, a scintillating fiber detector will be placed immediately downstream of CEDAR2, to confirm/support the effective beam matrix for the beam track extrapolation from the AMBER beam telescope up to the CEDARs location. The data collected during this test will then be analyzed to further optimize the kaon and pion identification efficiency for the long Drell-Yan production run at high beam intensities. This test should also allow to confirm the effective transport matrix. The simulation of the beam optics might then be revised to identify the origin of discrepancies. In addition, we are also exploring possibilities of further improving beam divergence measurement by adding a dedicated silicon beam telescope detector.

## 5.3 Further future improvements to the M2 beamline

Drell-Yan is a rare process, and the AMBER goals in terms of statistical accuracy require the highest beam intensity possible. The present configuration of the T6 primary target and the M2 beamline would allow for an increase in beam intensity, from the  $3.5 \times 10^8$  to  $4.8 \times 10^8$  particles/spill. The former number, which is the nominal intensity also used for the COMPASS Drell-Yan measurements, is imposed by radio-protection safety rules. Thus, improved shielding in the AMBER experimental hall may allow to increase the beam intensity at the AMBER target. Such optimisation studies are ongoing, done by the CERN Radioprotection group. Preliminary results shown by Claudia Ahdida at the PAW 2024 Workshop this year show that improved shielding may allow for an increase in the beam intensity in EHN2 by a factor 2.8, still keeping the prompt radiation doses within the allowed limits (see figure 17).

The beam particle identification efficiency is another aspect where further improvements are foreseen. Kaon tagging efficiency is very much dependent on the beam divergence at the CEDAR location.

Optimal efficiency is achieved for angles below  $60 \mu\text{rad}$ , while the present divergence is at least a factor 3 worse, which is due namely to multiple scattering along the beamline. In the M2 beamline there are sections corresponding to 80 meters of air, including 9 scrappers. Studies done by the BE group are ongoing, that show an improvement in kaon transmission (5%) when vacuum is implemented in the air sections (implementing vacuum also to the scrappers region would increase this to 20%, but this is technically challenging and costly).

Color scale according to area classification

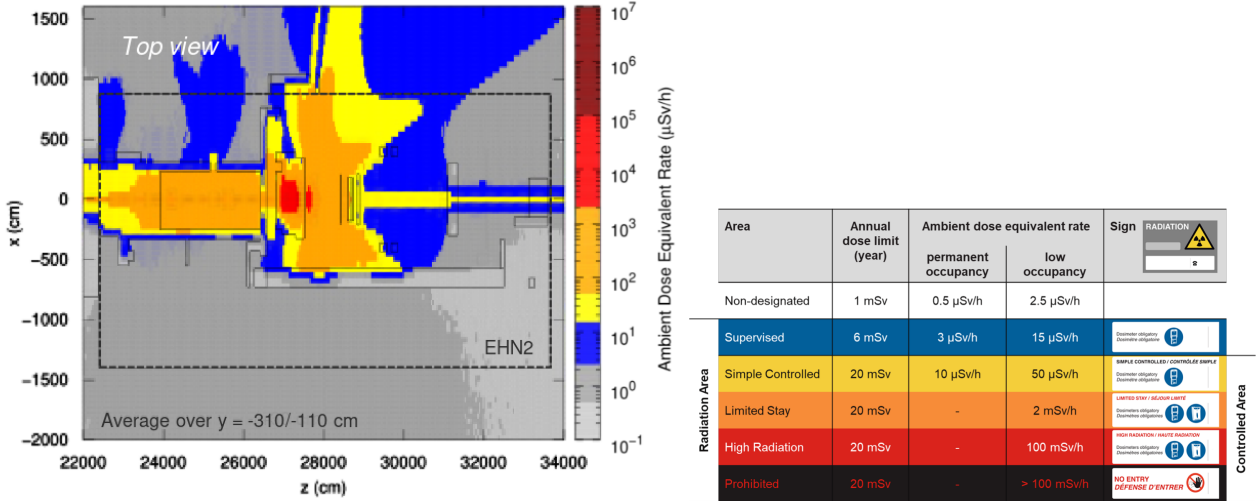


Fig. 17: Simulation of the radiation doses in the EHN2 hall and surrounding area, using an hadron beam of  $1 \times 10^9$  particles/spill (Claudia Ahdida, PAW'2024 Workshop). The color code used on the left is the same as used for the RP areas classification, shown on the right.

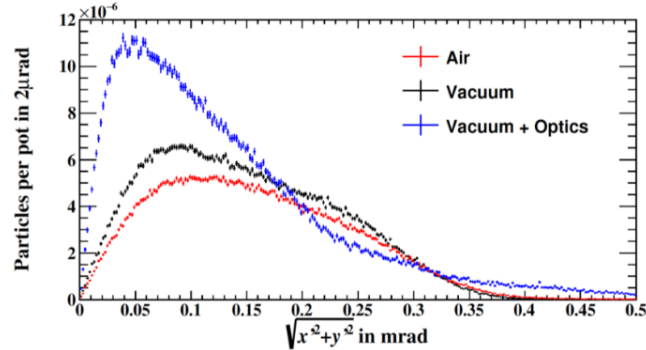


Fig. 18: Studies for an upgraded M2 beamline, including vacuum and modification to the collimation (Dipanwita Banerjee, PAW'2024 Workshop).

Improvements to the beam optics also allow to reduce the beam divergence in the horizontal plane, to reach about 50  $\mu$ rads. Overall, these preliminary studies, shown by Dipanwita Banerjee at the PAW'2024 Workshop, indicate that the beamline upgrades planned will increase the kaon flux reaching the AMBER target to  $6 \times 10^6$  kaons/spill. This is illustrated in Fig. 18, presented by Dipanwita Banerjee (BE group) at the PAW'2024 Workshop.

## 6 Hardware

### 6.1 The Liquid Hydrogen/Deuterium target for APX

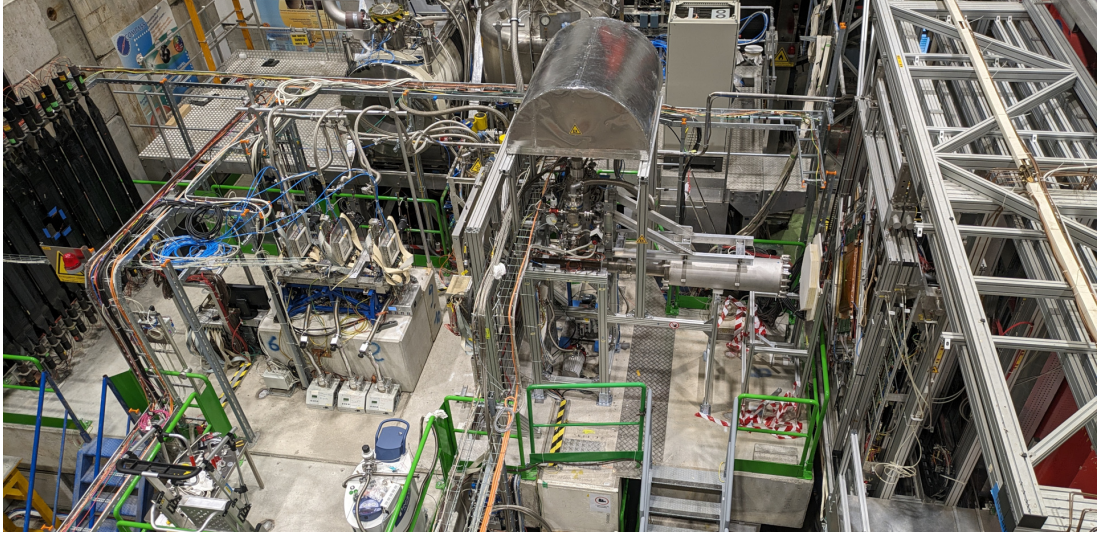


Fig. 19: Picture of the APX 2024 target region. The beam is arriving from the left-hand side. Afterward the beam is measured by several SciFi and Silicon stations before it is impinging on the  $\text{LH}_2/\text{LD}_2$  target on the right and afterward entering the two-stage AMBER spectrometer.

For the Antiproton Production Cross-Section Measurements (see section 2) a new liquid hydrogen/deuterium target system had to be developed (Figure 19). This development was done in collaboration with the TE-CRG and EP-DT-DI departments at CERN. Initially, the plan was to re-use the existing liquid hydrogen ( $\text{LH}_2$ ) target system, which had been used in 2016 and 2017 at COMPASS, with small modifications for the APX program in 2024. However, early discussions in 2023 with the EP and HSE safety departments showed that besides the modifications of the target cell and the insulation vacuum chamber around the target cell, the old control system and the general infrastructure had to be completely newly designed to obtain clearance to operate the hydrogen target in EHN2. These necessary safety modifications led to about 5 weeks of delay in the operation of the new hydrogen/deuterium target system since the safety discussions and resulting definitions in the form of a comprehensive risk assessment took time until the end of March when they were released. This late release of the risk assessment delayed especially the planning and construction of the new safety and control system for which the released risk assessment was essential. A list of the different changes can be found below:

**Target Cell** The target is required to be 140 cm long with 4 cm in diameter. The cell material had been discussed with TE-CRG since September in 2023. The Kapton material target cell with 0.125 mm thickness, which was produced in 2017 for the COMPASS target, was chosen after the pressure test in February 2024. The pressure test showed the maximum pressure of the hydrogen is 1830 mbar with a safety factor of three.

**Target Vacuum Chamber** The target vacuum chamber for the new target cell is made of stainless steel pipe of 3 mm thickness with 323.9 mm in diameter to fit the acceptance of the AMBER spectrometer, and Mylar 0.35 mm thickness is applied for the downstream window. The design and construction of the chamber were done by TE-CRG. Because of the large vacuum chamber, it was also important to design the support structure of the refrigerator. Thanks to BE engineering support, the structure was installed in the experimental hall before the installation of the refrigerator on April 22nd.

**PLC Safety and Control system** The new PLC safety and control system was required to monitor different process parameters and take action in case of detection of a hydrogen leak in the form of releasing the hydrogen or deuterium gas and switching off all non-ATEX equipment in the proximity of the hydrogen circuits. For this, the system had to be equipped with ATEX-certified vacuum pumps and pneumatic remote valves. Also, the whole instrumentation had to be reviewed and sensors had to be exchanged in

case an ATEX-certified alternative exists. Existing sensors with ATEX certification had to be equipped with certified ATEX barriers in addition. All safety-relevant functions had to be covered by a SIL-certified safety relay. After the release of the explosion risk assessment of EP-Safety and HSE on March 27, a work package of the PLC system with EP-DT-DI was established. The PLC system controls the pumps, the helium cryocooler, and the liquid hydrogen pressure control by PID as well as interlocks of the equipment and the safety actions.

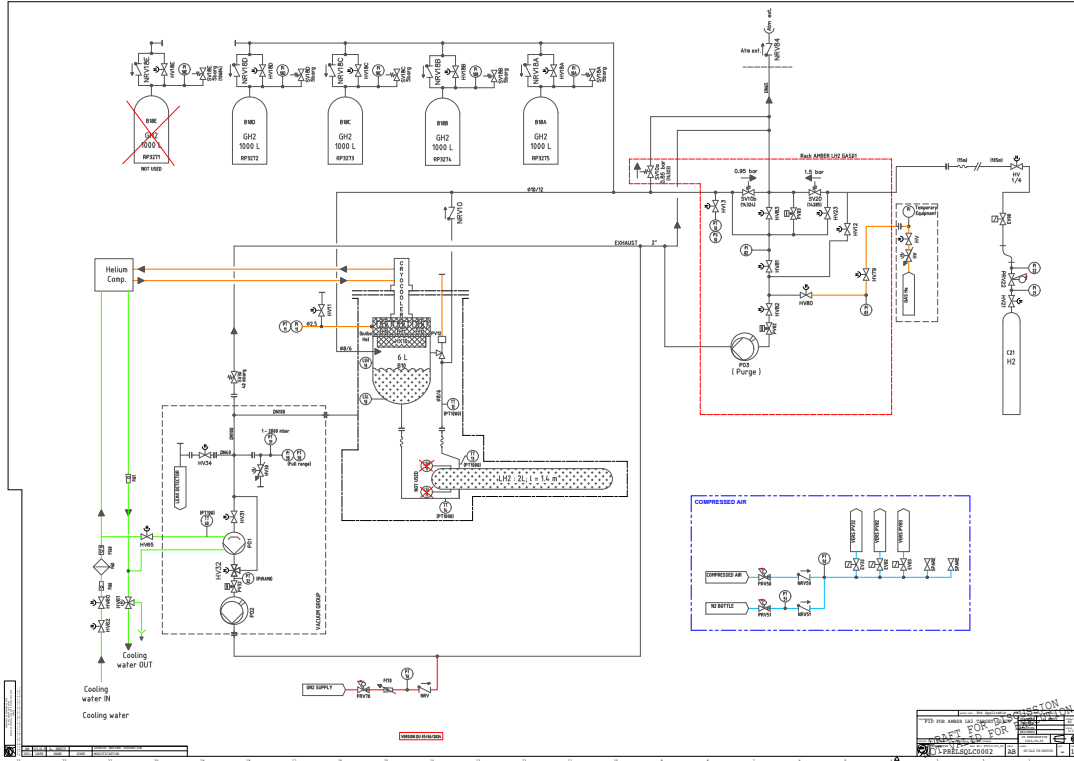


Fig. 20: Piping and instrumentation diagram of the  $\text{LH}_2/\text{LD}_2$  target

The full PID of the system is shown in Figure 20. The leak checks of the insulation vacuum, the hydrogen line, and the hydrogen exhaust line were performed after the installation of  $\text{LH}_2$  system. The hydrogen space was purged by helium gas three times at the end of May. The system as shown in Figure 19 was fully operational after the PLC safety test organized by the EP safety group passed on June 6. The target cell and the  $4 \times 1000$  liter hydrogen buffer volume gas tanks were filled by the hydrogen gas (Figure 20). The initial pressure of the gas was 1750 mbar which was below the allowed maximum pressure of 1830 mbar mentioned above. On June 8th the hydrogen liquefaction was started by the cryocooler. It took more than 14 hours to stabilize the hydrogen vapor pressure at 1150 mbar that included the PID control commissioning as it is shown in Figure 21. After stabilization the system was able to keep the pressure stabilized at  $\pm 1$  mbar. This resulted in a enough stable operation to obtain a  $\text{LH}_2$  temperature of 20.7 K. This temperature corresponds to the density of  $70.2 \text{ kg/m}^3$ . Afterward, the system was also used as a liquid deuterium ( $\text{LD}_2$ ) target. For this the hydrogen was purged and the system was refilled with deuterium. After successfully cooling down the controlled vapor pressure was 1130 mbar which corresponds to a deuterium temperature of 24.0 K and a density of  $162 \text{ kg/m}^3$ . The change over from  $\text{LH}_2$  to  $\text{LD}_2$  took place from June 30 to July 2. Afterward, the system was running without problems until the end of the APX beam time with the deuterium pressure stabilized again at  $\pm 1$  mbar.

## 6.2 CEDAR Detectors

The CEDAR detectors are essential components for the beam PID for the APX and DY programs. The BE-EA and SY-BI departments performed a major refurbishment program after the identified issues with the CEDAR detectors during the 2023 APX beam time and DY test. This included recovery of the so-called pulsed motion mode for controlling the diaphragm and cedar positioning system, as well as a full refurbishment of the gas,

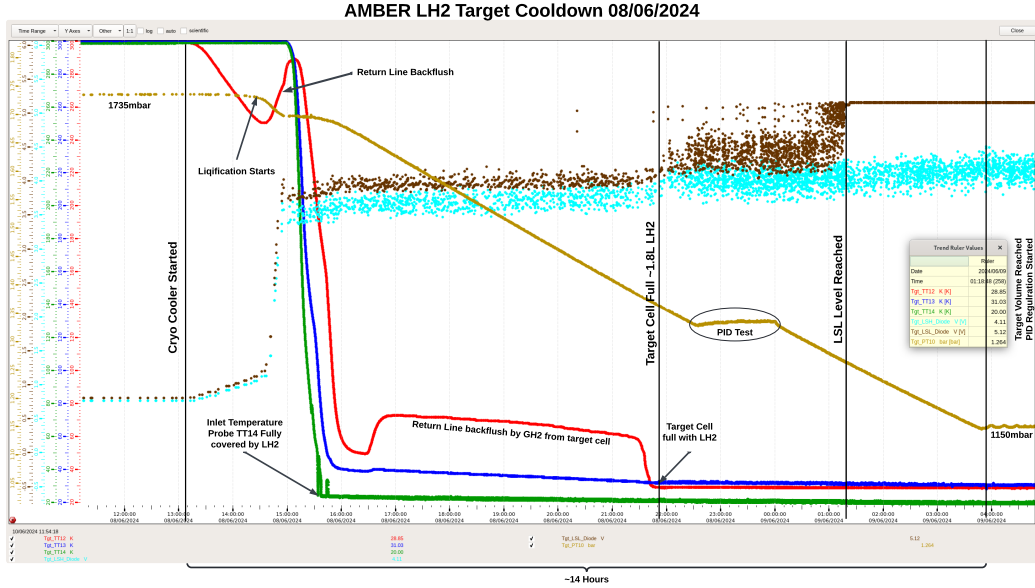


Fig. 21: Cooldown of the  $\text{LH}_2/\text{LD}_2$  target filled with hydrogen on 08.06.2024 .

optical, and mechanical systems of both CEDARS. A summary of the issues and mitigations can be found in [10].

On the AMBER side, the following modifications were implemented to facilitate servicing and stable operation of the electronics, as well as to improve its performance:

- Readout electronics were moved from the beam line location, which is not accessible during beam operation, to the barrack 888-R-003, to allow better access for intervention and remove the electronics from the high radiation region of the beam line.
- The twisted pair cables connecting the PMT bases to the readout electronics were replaced with ones with thicker conductors (AWG23), resulting in lower attenuation of the signals.
- The pre-amplifier circuit in PMT bases was modified and the gain was increased by a factor of two. This change did not affect the PMT pulse shape at the output of the base, since the amplifiers had sufficient bandwidth and slew-rate margins.

Since it was identified that the main noise contributions come from electromagnetic interference issues originating in the readout crate, the last two of the above changes resulted in improved signal-to-noise ratio (SNR) achievable at the input of the discriminators. This, in turn, results in better readout efficiency, as it allows to set lower threshold levels in relation to the average amplitude of the single photoelectron response of the photomultiplier tubes. In addition, the timing resolution should also be improved, since the time-walk effects will be diminished, and also there is an improvement in the ratio of the leading edge time to the SNR. Fig. 22 presents an example of the measured single photoelectron response.

After the full consolidation, both CEDARS were moved from the gray room in EHN1 back to the beam position in EHN2 on 15th March. During the beam line commissioning by BE first hints came that especially CEDAR 2 is misbehaving. It was not possible to align CEDAR2 by the traditional alignment method over the count rates of the eight photomultipliers. After the end of the beamline commissioning, further intensive and detailed studies were performed by AMBER. This exercise was only possible due to the improvements in the CEDAR positioning control system. During this studies, overall alignment of the CEDAR and photomultiplier issues were excluded.

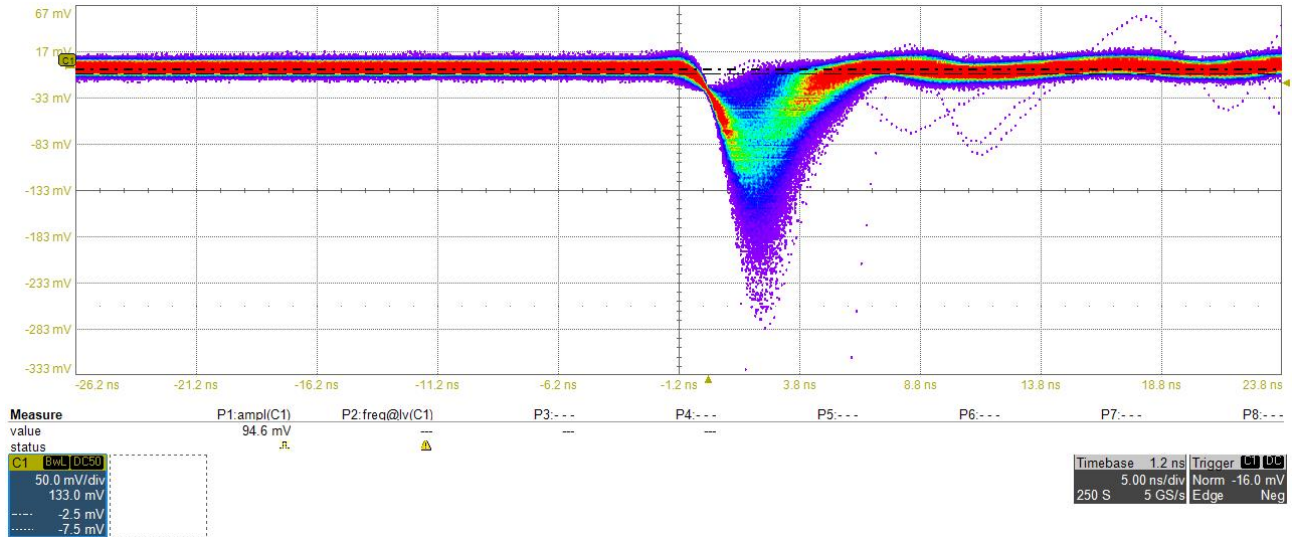


Fig. 22: Example persistence-mode plot of a single photoelectron response of one of CEDAR’s PMTs (CEDAR 1, PMT 4, sum of four channels). Note that for a single channel, the noise will be a factor two smaller, since the sum output from the discriminator contains noise from the pre-amplifier from all four channels. The PMT gain was  $5 \times 10^5$ , which is the value recommended by Hamamatsu for the tapered-divider configuration.

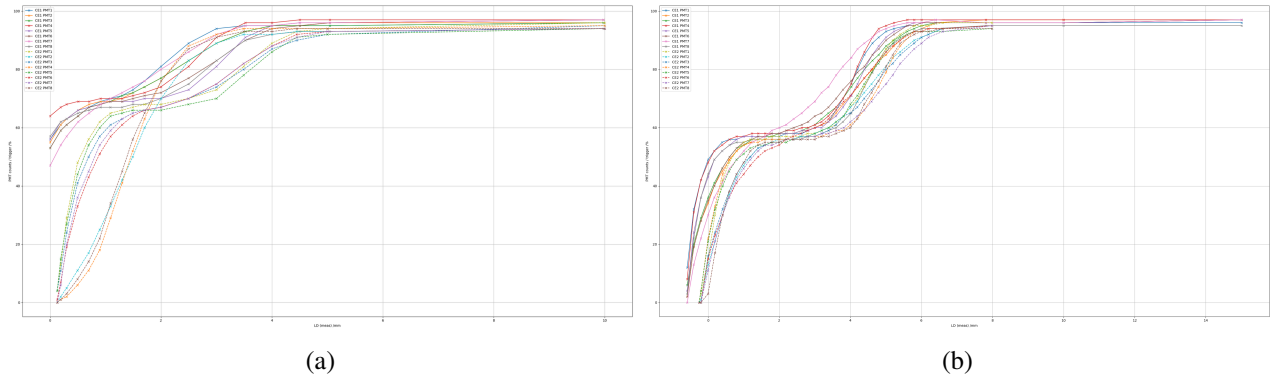


Fig. 23: In (a) The diaphragm scan of CEDAR 2 before the intervention is shown which clearly shows a set of three PMTs with different behavior than the rest. In (b) The behavior of all PMT channels of CEDAR2 is similar.

Several diaphragm scans pointed to an optical misalignment of the optics or diaphragm of PMT positions 2/4/8 as shown in Figure 23(a). After this conclusion, it was decided to remove CEDAR2 again on 25th April from the M2 beamline and perform further investigation in the gray room. After meteorological studies, a new alignment tool was produced which was used to improve the circularity of the diaphragm opening. After re-installation of CEDAR2 on 08th May it could be confirmed that these adjustments improved the behavior of CEDAR2 as shown in Figure 23(b). The figures still show a few outliers, but for the identification of protons during the APX the performance was sufficient. The planned DY high-intensity test of the CEDARS was postponed to the October beam time which allows for another round of consolidation during the summer.

### 6.3 TPC and Gas System

#### 6.3.1 Beam test of the IKAR TPC in 2023

IKAR TPC detector is considered as a prototype for the main TPC. Many aspects of functionality and performance can be tested with the IKAR TPC and used to optimize the main detector. A beam test with muons was

performed with the IKAR TPC in October 2023. The detector itself, corresponding electronics, DAQ, vacuum system, and gas system were assembled and commissioned starting in August 2023. A photo of the setup on the beam position is shown in Figure Fig. 24. Many improvements related to the safety system have been implemented as well - hydrogen lines, alarms et cet. The gas filling system for the TPC has been assembled at the new location with respect to the previous test in 2021. New gas pipes were installed along the beam line

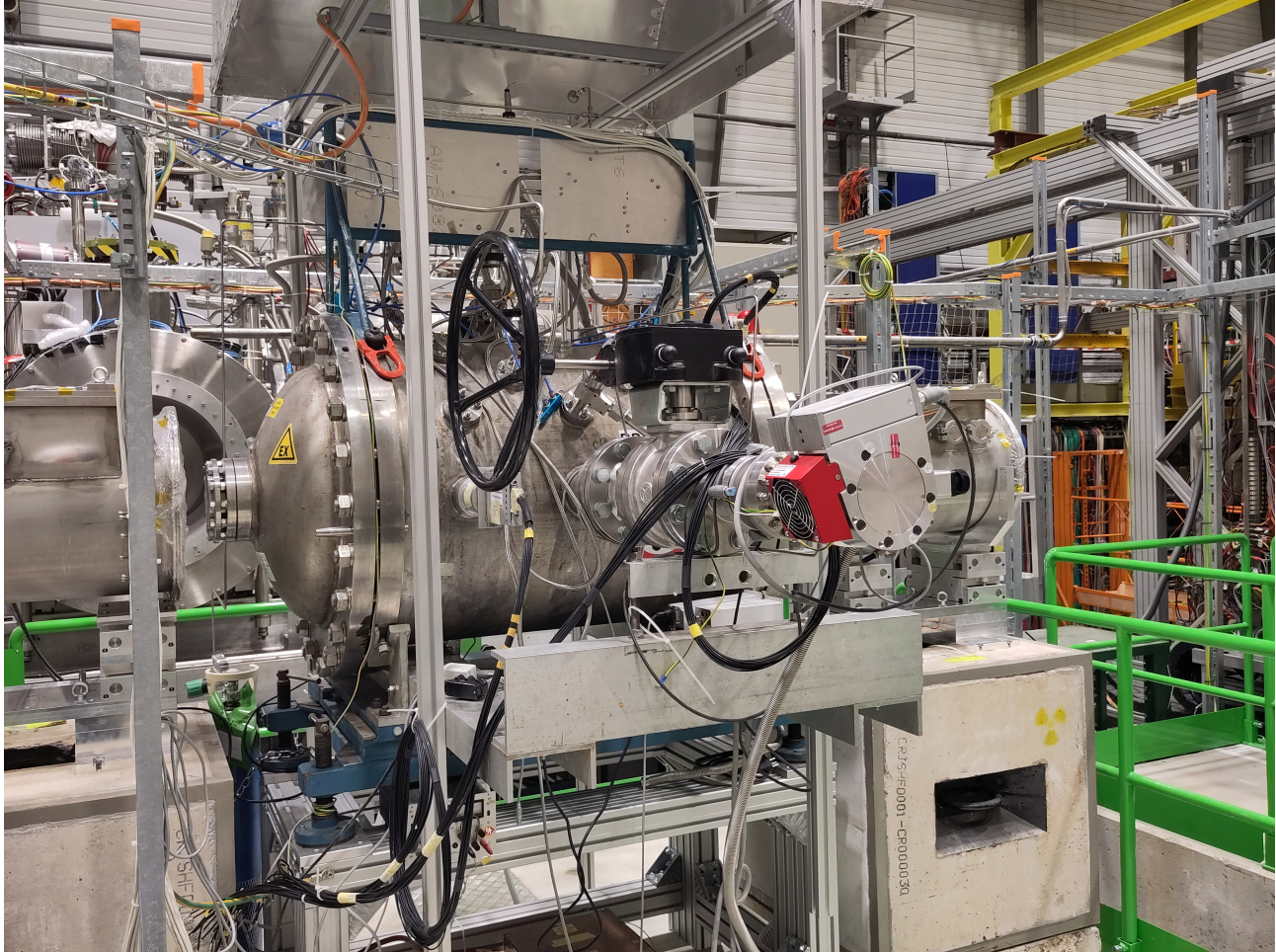


Fig. 24: IKAR TPC in the target area.

towards the target area and the TPC location. The IKAR TPC was operated at a maximum pressure of 8 bar. The gas system was upgraded having an additional gas purification system and thus, the impurities ( $O_2$  and  $H_2O$ ) could be kept to a level below 1 ppm. The absolute calibration of all channels of the pre-amplifiers has been performed allowing best measurement of the energy of recoil protons. Muon beam with intensities up to  $10^7$  per second has been provided for the test.

### 6.3.2 Preparation of the main TPC

The new two-cell TPC which is considered as main for the PRM experiment has been designed. The design is modular, allowing for an extension to the four-cell detector. The pressure vessel together with the middle flange is produced by the company from Denmark. Several parameters are improved with respect to IKAR TPC. The anodes will have a diameter of 600 mm covering a larger range of protons, the total drift length per cell is 400 mm, the reachable gas pressure will be increased by more than a factor of two. All this will provide at least twice larger statistics during the experiment as in the case of IKAR TPC. In Fig. 25 a 3D model of the main TPC with the middle flange and 10 smaller flanges for the pre-amplifiers and HV connectors is shown. Overpressure test up to 32 bar of the whole construction has been successfully performed and a CE-certificate provided assuring the safe operation up to 20 bar of hydrogen or other gas.

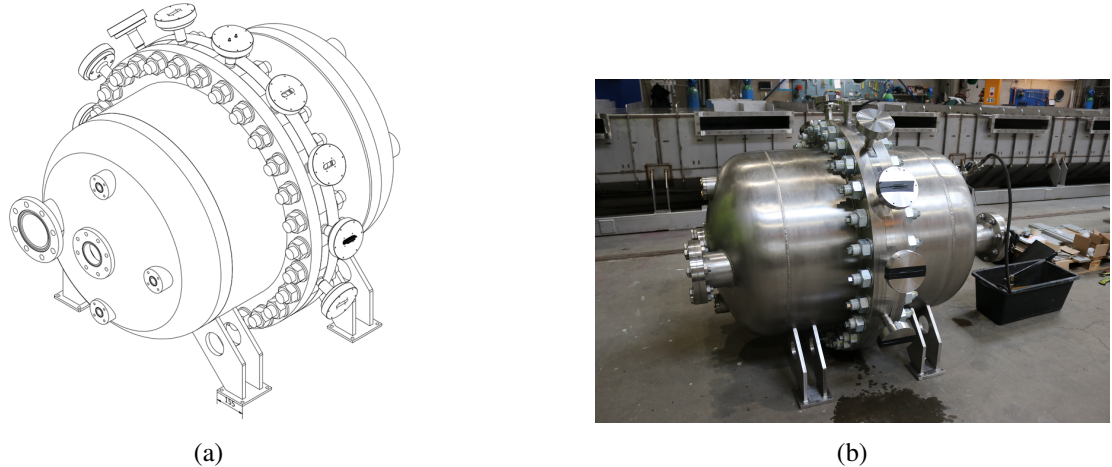


Fig. 25: In (a) a 3D model of the main TPC is shown. A photo of pressure vessel including middle flange shown in (b).

Taking into account the design of the existing preamplifiers, new devices are developed. They have power regulation on board allowing lower noise levels and more recent versions of the components. The PCBs are produced and will be assembled in September 2024. A new set of inner elements is designed – field correction rings, cathode and grid support rings, isolation rings between the middle flange and grid support rings, and isolating screws between all these elements Fig. 26. The new grid PCB and the anode plane PCB are designed based on Monte Carlo simulations. Different to IKAR TPC, not a usual PCB material will be used but a Rogers Series 4000 substrate, typically used for high-frequency devices like radio antennas. It has better surface quality and much lower outgassing as a standard PCB material like FR4. Part of the elements are obtained, others are ordered and will be available in September 2024.

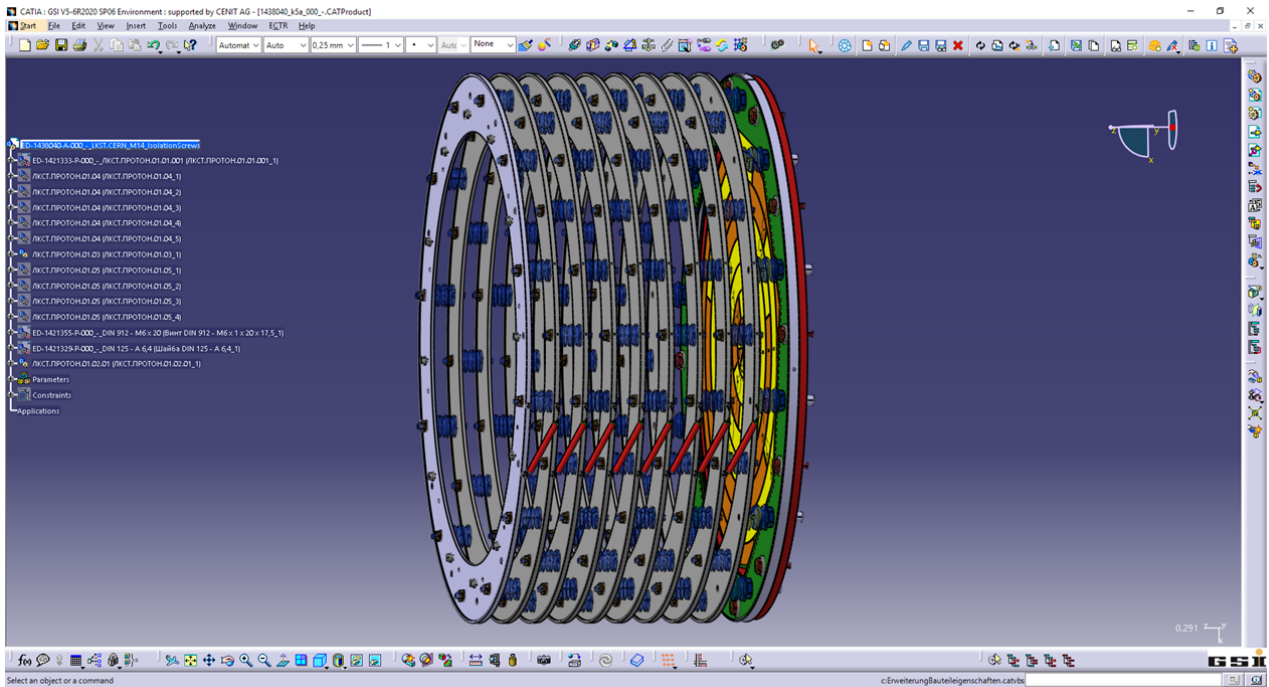


Fig. 26: CAD drawing of the TPC inner electrode structure.

In order to fulfil very high requirements to the gas purity inside the detector, it is not enough periodically filling new gas as it has been done in case of IKAR TPC. New gas system with permanent circulation and cleaning has been designed Fig. 27. It supports a required pressure and gas flow. The most important (from the experimental point of view) parameters are pressure and the temperature and they are controlled by several sensors. In order

to know the correct temperature of the gas, one more temperature sensor will be inserted into the middle part of the TPC pressure vessel. Additional important parameters (from safety point of view) like amount of water and oxygen in the gas, as well as a presence of hydrogen in the air are controlled by the corresponding sensors. All parameters of the gas system will be readout and steered by a dedicated PLC system.

The whole detector and the gas system, due to the usage of hydrogen, have been evaluated by the external company and the risk assessment document produced. Several requirements and recommendations are taken into account for the design of the detector systems and surrounding elements.

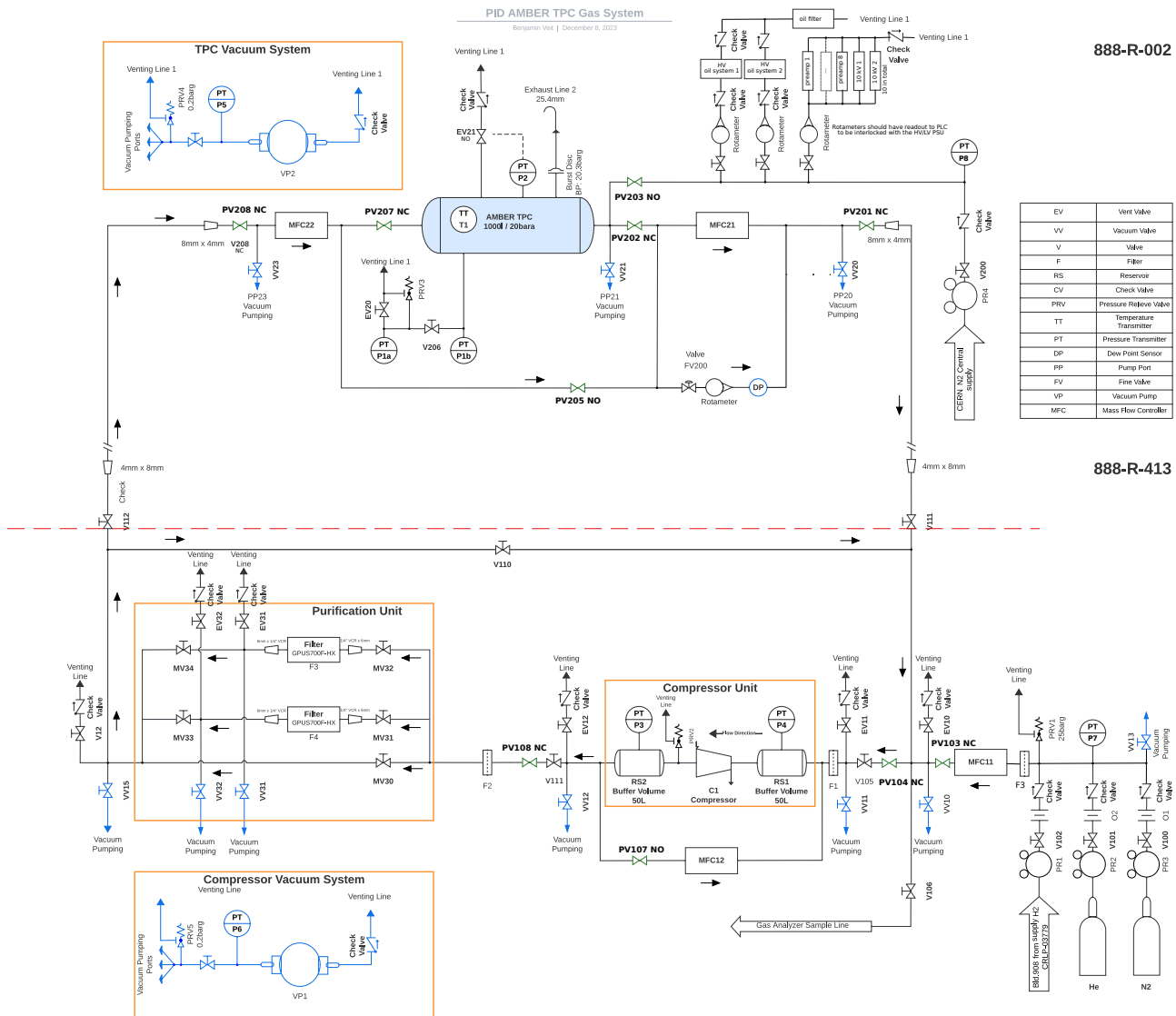
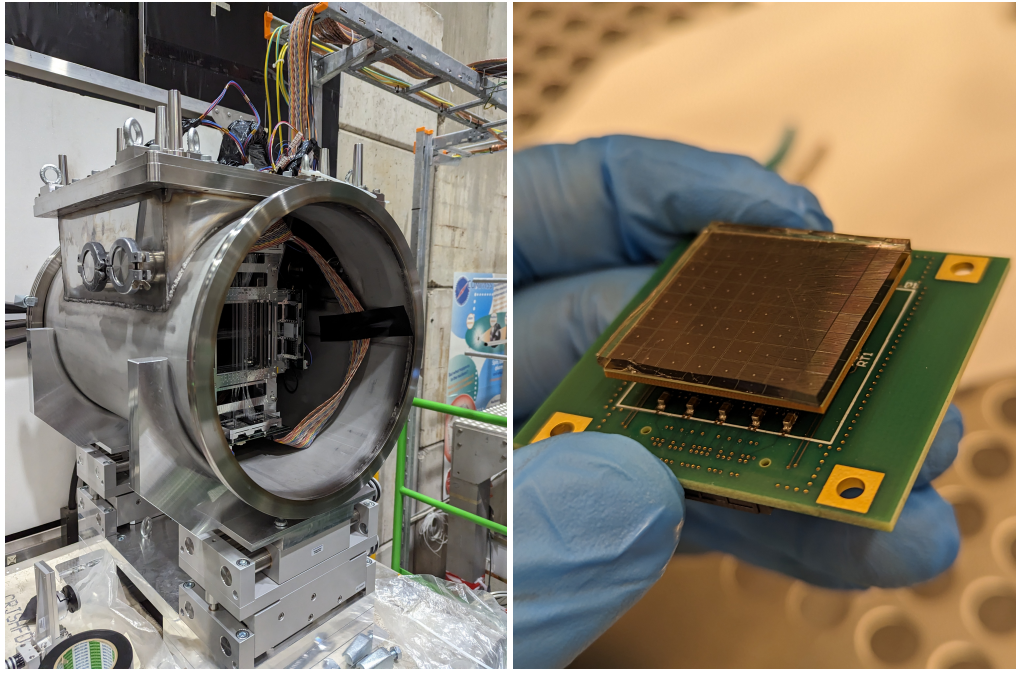


Fig. 27: TPC gas re-circulation and cleaning system.

The choice of the elements for the gas system is made taking into account the functionality and requirements according to the risk assessment. The elements are being procured and the whole system is supposed to be put together in Autumn 2024.

## 6.4 Unified Tracking Station UTS

A combination of Silicon Pixel Detectors (SPD) and Scintillating Fiber Hodoscopes (SFH) measure the trajectories of the scattered muons and the muon scattering angle. Three layers of ALPIDE MAPS sensors are used together with four scintillating fiber planes in one Unified Tracking Station (UTS). All detector vessels have been set up for the beam test in September 2023 and the alignment system has been commissioned successfully.



(a) UTS with SFH prototype in the target area. (b) Gel pad used to improve the SiPM-fiber coupling in the SFH prototype.

Fig. 28: Beam test in October 2023: UTS station and gel pad installed in SFH.

One of the UTS stations together with the SFH prototype is shown in Fig. 28. Progress on individual detector systems is presented in the following subsections.

#### 6.4.1 Scintillating Fiber Hodoscope (SFH)

The Scintillating Fiber Hodoscope consists of 500  $\mu\text{m}$  thick scintillating fibers, which are read out with 8x8 SiPM arrays. A dedicated beam test with a detector prototype was performed in June 2023 using the MSADC system, with the first results already shown in last year's report [2]. In addition to previous results, a first estimation of detector efficiencies has been performed with this data. A homogeneous detection efficiency of more than 99 % can be achieved with less than 100 background hits per second per channel for both mirrored fibers as well as double-sided readout, as shown in Fig. 29. The background hits originate from dark counts in the SiPM arrays, the dark count rate strongly depends on the operating temperature which was above 40  $^{\circ}\text{C}$  during the test. A water-based cooling system, which will further reduce the dark count rate is currently in preparation and foreseen for testing in October.

In October 2023, the prototype was tested in the target area with nominal PRM beam conditions and additionally with high-intensity muon and hadron beams. We also installed silicon gel pads to improve the coupling of the scintillating fibers to the SiPM arrays.

A prototype of a new detector readout is currently in production, with a beam test scheduled for October. It is based on the Citiroc 1A ASIC and a modified version of the AMBER iFTDC and will be compatible with the streaming DAQ described in Sec. 6.8.

#### 6.4.2 Silicon Pixel Detector (SPD)

**ALPIDE Detectors Front-end Electronics** The ALPIDE pixel detectors (see Section 6.4.2) feature several readout modes, out of which the one that will be used in AMBER is the high-speed serial link, at 1.2 Gbps. The hardware developed at the University of Freiburg for this purpose makes use of a Kintex-7 Xilinx FPGA to read out each group of six chips, taking advantage of the FPGA transceivers that work very efficiently at these data rates and allowing for additional tuning of the channels.

The first prototype boards for the ALPIDE data acquisition system were produced in 2021 and have been tested

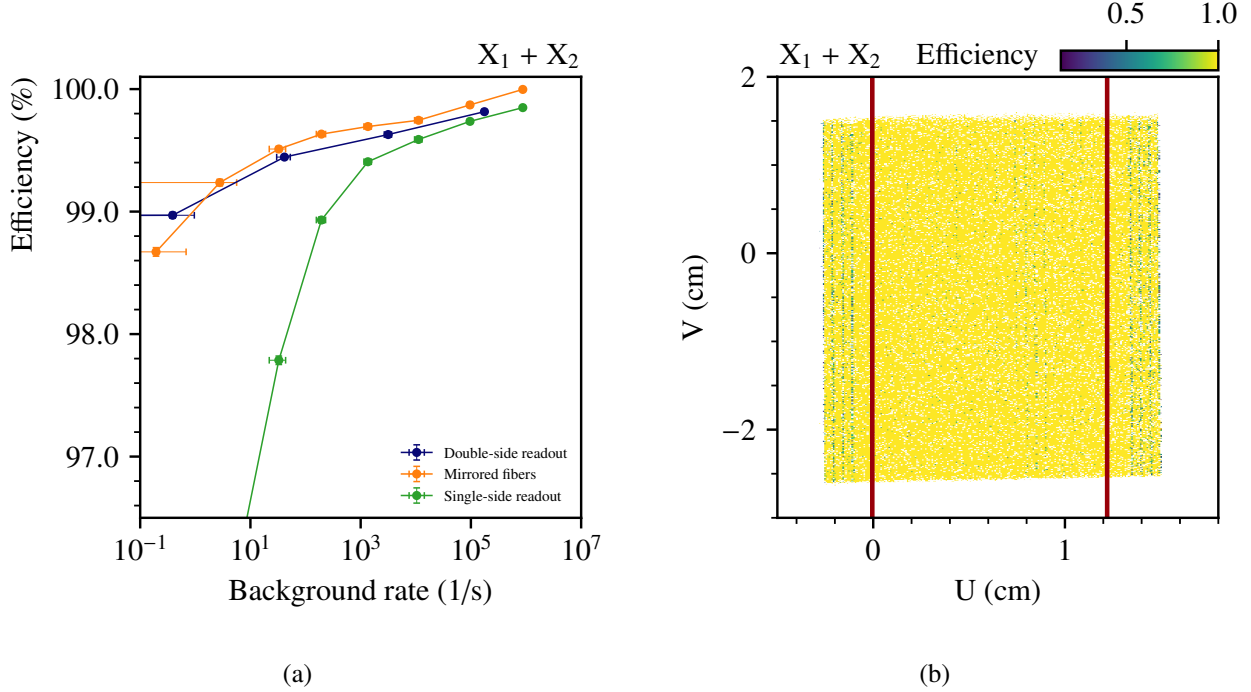


Fig. 29: SFH detection efficiency requiring at least one hit in one of the two X planes. Fig. (a) shows the efficiency versus the background rate from dark counts depending on the threshold. In Fig. (b) the position dependence of the efficiency is shown for double-sided readout for hits with at least three fired SiPM cells. The red lines indicate the combined active area of the planes. [11]

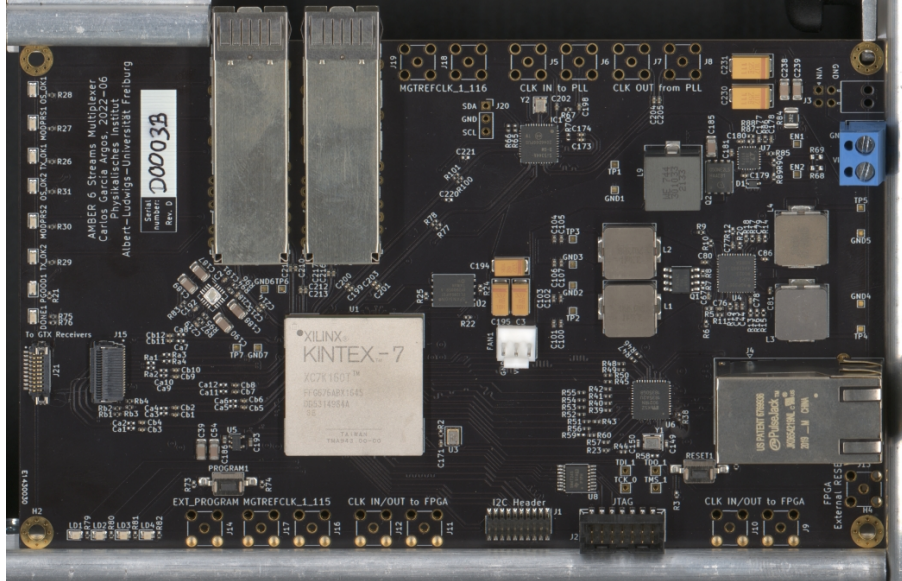


Fig. 30: Prototype of the ALPIDE Detector Specific DAQ Board (CMUX).

in lab conditions with individual as well as multiple detectors, with no interface to the AMBER DAQ system. The boards include the required connections to communicate with the six ALPIDE detectors, an Ethernet interface for external control, internal clock generation, two optical interfaces for fast data transmission, and other configurable input/output connections. One of the assembled prototypes is shown in Fig. 30.

The tests performed on the hardware include verification of the signal integrity at the 1.2 Gbps data rate for the ALPIDE detector part, and up to 10 Gbps for the optical transmission and reception side. In addition, the multi-drop busses for the control and clock lines connecting up to six ALPIDE chips were checked.

The firmware implementations include the following features:

- Control of the clock generator to configure the frequencies for the FPGA transceivers.
- Data readout from the transceiver lines coming from the ALPIDE chips, and processing for further transmission.
- Clock generator (40 MHz) and control interface to the ALPIDE chips, for register read/write.
- Data output to SFP+ transceivers, with various protocols: UDP on 10 GbE or UCF utilizing 8b10b encoding.
- IPBus interface, as an integrated part of UCF interface, to control the FPGA or the ALPIDE chips, and read out their statuses.
- Debug blocks using Virtual I/O and Integrated Logic Analyser.

The initial development of the firmware lacked direct access to the real chips, which slowed down testing substantially.

Additional supporting hardware for the ALPIDE part of the DAQ has been designed and produced:

- FMC to Firefly and SFP+: an FMC daughter card with two Firefly connectors (one for transmission and another for reception) and one SFP+ cage, that was used for the initial firmware development, by allowing the transmission of synthetic ALPIDE data from a separate commercial FPGA board.
- Telescope Carrier: a card interfacing with ALICE’s single chip carrier cards, for up to 9 ALPIDE chips using the PCI Express connector.
- TCS Receiver: a card featuring a clock and data recovery chip that allows interfacing with the TCS controller.

Currently, integration tests with the AMBER DAQ are ongoing at CERN. The setup consists of the CMUX card, using the aforementioned TCS receiver add-on card, and a single ALPIDE detector. The CMUX interfaces with the TCS controller, the DHMux, and the IPBus network.

## 6.5 New Large Area Micromegas detectors

The present state of the MultiWire Proportional Chambers (MWPC) of AMBER requires that a new detector to substitute some of the stations is designed and produced for future running. The chosen technology to substitute the most aged MWPCs is the Micro-Pattern Gaseous Detectors (MPGD), specifically a resistive bulk MICRO-MEsh-GAseous Structure (micromegas) detector.

To have the same active area of roughly  $1 \times 1.5m^2$  as the MWPCs and limiting the R&D’s technological risks a three separate adjacent large-area micromegas modules configuration was chosen. Each module has two readout planes in a face-to-face configuration and a common cathode providing an XUV space measurement. For the lateral modules, a uniform  $10M\Omega/sq$  Diamond-Like Carbon (DLC) layer will be deposited above the readout strips, whereas the central module is planned with a double resistive layer configuration. The concept is depicted in Fig. 31.

Main parameters of the future detector are summarized below:

- Size:  $1 \times 1.5m^2$ ;
- Rates per channel:  $< 500$  MHz/stripe (passivated center);
- Spatial resolution:  $600\mu m$ ;

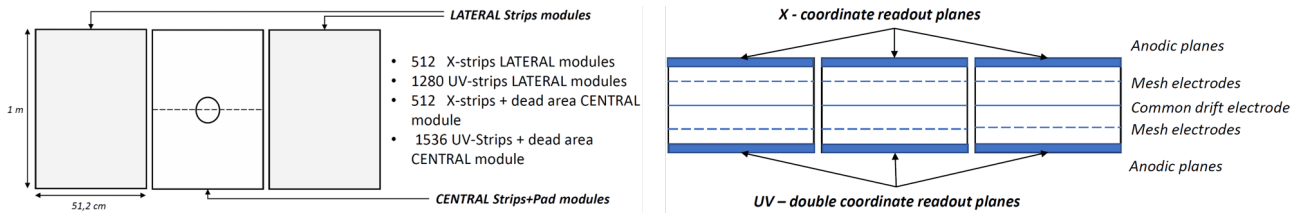


Fig. 31: A frontal and top view of the MM concept.

- Time resolution: 3 – 5 ns.

The design of the small micromegas prototype detectors to study the concept and the FE integration has been carried out by the INFN Torino group and previously tested at various test beams. The first full-size prototype module has been designed by the MPT Workshop at CERN in close collaboration with INFN Torino, and it is being presently produced at the MPT Workshop with the aim to be ready for testing in October 2024 at AMBER. The readout plane layout for the first prototype module are shown in Fig. 32. Fig. 34 alongside the first micromegas detector model shows the temporary mechanical structure intended for use in the October test setup, designed to position the detector centered at a beam height of about 3.150m with a possibility of a horizontal movement to tune the final positioning.

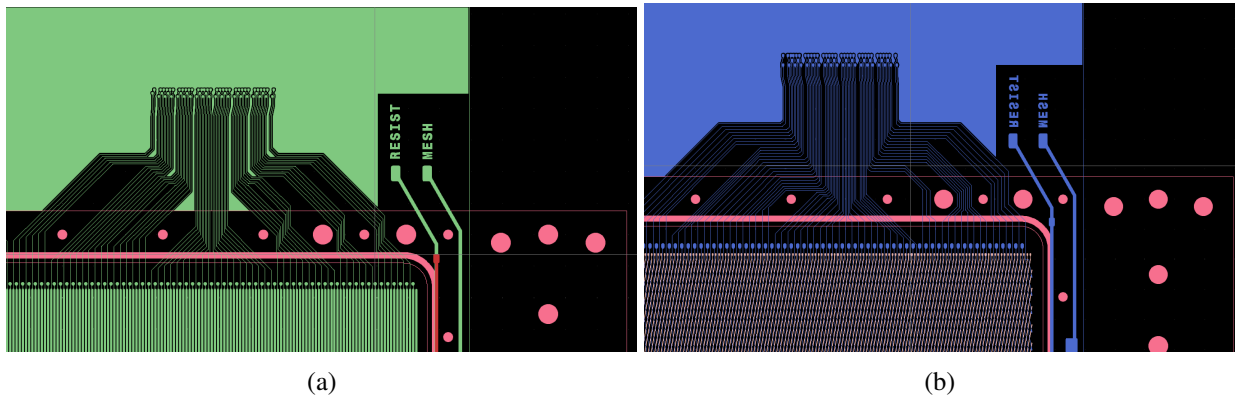


Fig. 32: Gerber files for the PCBs layout of the readout planes. (a) for the X-coordinate and (b) for the UV-coordinates.

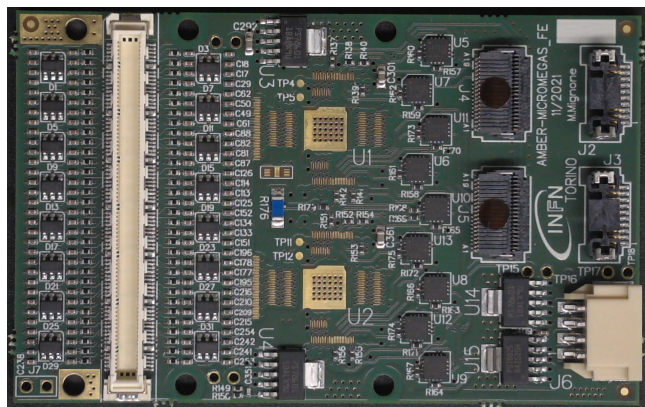


Fig. 33: AMBER micromegas front-end board developed by INFN Torino.

Leveraging on the results and experience gained from prior tests, a TIGER (Torino Integrated GEM Electronics for Readout) based front-end will be employed in a stand-alone DAQ configuration for the first test of the full size prototype lateral module in laboratory and on beam. The front-end board (FEB), that was specifically

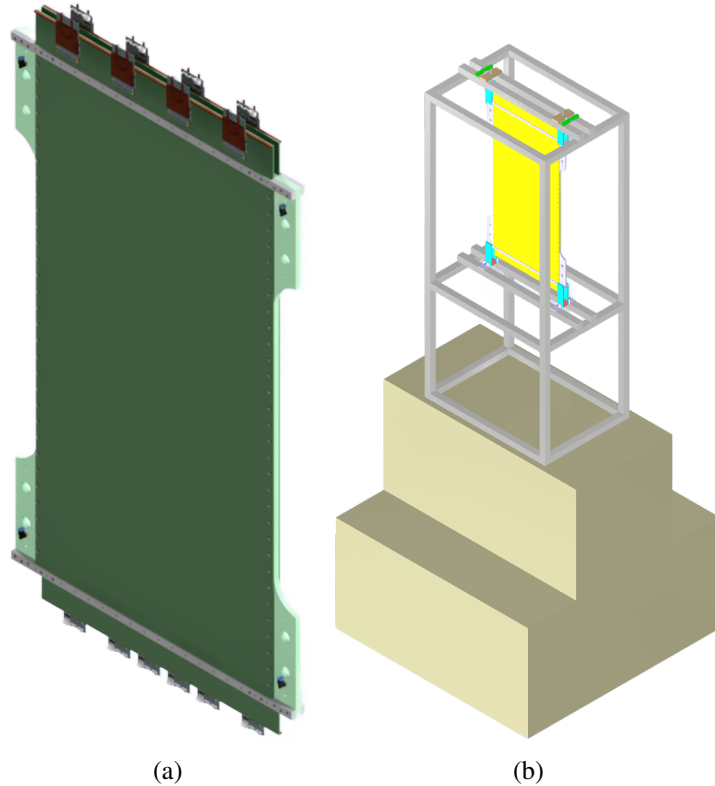


Fig. 34: 3D model of the first MM detector module (a) and the mechanical structure for the October 2024 test in AMBER experimental hall (b)

designed and developed for our application by INFN Torino, features a new form factor adapted to the detector, an enhanced Electro-Static Discharge (ESD) protection circuit, and upgraded data transmission connections allowing for a full speed operation of the TIGER ASIC.

In parallel with the detector development, an micromegas and wire chambers optimized new front-end electronics (FEs) is being designed to meet both the detectors and future trigger-less DAQ requirements. For these FEs a new 64-channel Application Specific Integrated Circuit (ASIC), namely Torino-Readout for AMBER (ToRA) is in the design phase, it will feature the capability to have simultaneous time and energy measurements with an architecture tuned for both micromegas and wire chambers signals. The first version (ToRA V1) is expected to be produced within 2024.

## 6.6 GEM Detector Development

Due to their age, the GEM detectors of the first generation face several issues. Hence, the detectors are step-wise replaced by a new (3rd) GEM detector generation. For the anti-proton production cross-section measurement, an up-to-date version of the triggered APV-based front-end electronics was implemented with the new detectors (Section 6.6.1). The minimal setup for the PRM foresees three GEM stations with triggerless readout. This new streaming readout (Section 6.6.2) will also be required for the meson structure measurement by using Drell-Yan process.

### 6.6.1 New GEM detectors with triggered readout

After the initial installation of the new triggered GEM detectors in 2022, performance issues were identified. These issues have since been addressed in preparation for the antiproton production run in 2024, allowing for the installation of two full stations (four detectors) equipped with the new triggered front-end electronics.

Figure 35 shows the two new triggered GEM detector stations currently in their test position just behind Spectral

Magnet 2. This new installation in the AMBER spectrometer aims to demonstrate that the higher noise levels observed in the front-end system can be resolved in an experimental environment. Additionally, it aims to confirm that the detectors can deliver meaningful data for the experiment.



Fig. 35: Picture of the two new triggered GEM stations, installed just behind the Spectral Magnet two, for the AMBER antiproton production run in 2024.

Figure 36 illustrates the cluster positions for each projection recorded during an alignment run with one of the stations. The figure clearly shows a beam profile, indicated by the correlated 2D cluster positions. However, due to instability issues with some front-end electronic components, the detector has not operated consistently throughout the entire data-taking period. The sources of these issues have been identified and will be addressed in future periods.

The expected performance of the new detectors is comparable to, or even better than, the previous generation. Design adjustments have been made to improve rate capability and efficiency in specific regions of the detector. These properties will be evaluated during the analysis of the data acquired from this year's run, with results available soon.

### 6.6.2 Triggerless GEM readout

During the PRM test run in August/September 2023, a new GEM detector of the 3rd generation was fully instrumented with RD51 SRS-VMM electronics [12]. Figure 37 shows this prototype for the fourth-generation GEM detectors as installed on the AMBER spectrometer.

The SRS-VMM operated with excellent reliability and a large and complete data set was collected. Within the data analysis, the SRS-VMM was synchronized to the spectrometer using trigger signals coupled to an additional VMM front end board. Using reference tracks of the spectrometer serving as a beam telescope, both the detector and the VMM performance are currently evaluated. Data were collected for a variety of GEM gains, VMM preamplifier gains, and VMM thresholds to find the ideal working point for the final operation. The data analysis reconfirmed the reliable VMM operation and gain non-uniformities of the detector. Spatial and temporal residuals with respect to the spectrometer reference tracks are in the expected range. Although systematic evaluation of detector efficiency is ongoing, it has been preliminarily confirmed that sufficient detector efficiency above 95 % is reachable in detector regions without disturbances; see Figure 38. This indicates that the new GEM detectors can be operated at gains similar to those of the old GEMs. The triggerless readout is likely capable of maintaining a similar detection efficiency at low noise rates in a triggerless readout.

The development of custom triggerless frontend electronics, using the VMM ASIC and in a first stage also the RD51/DRD1 VMM frontend board has started. Compared to the VMM-SRS, the new scheme will use fewer materials and cables and be better integrated into the detector and the AMBER DAQ.

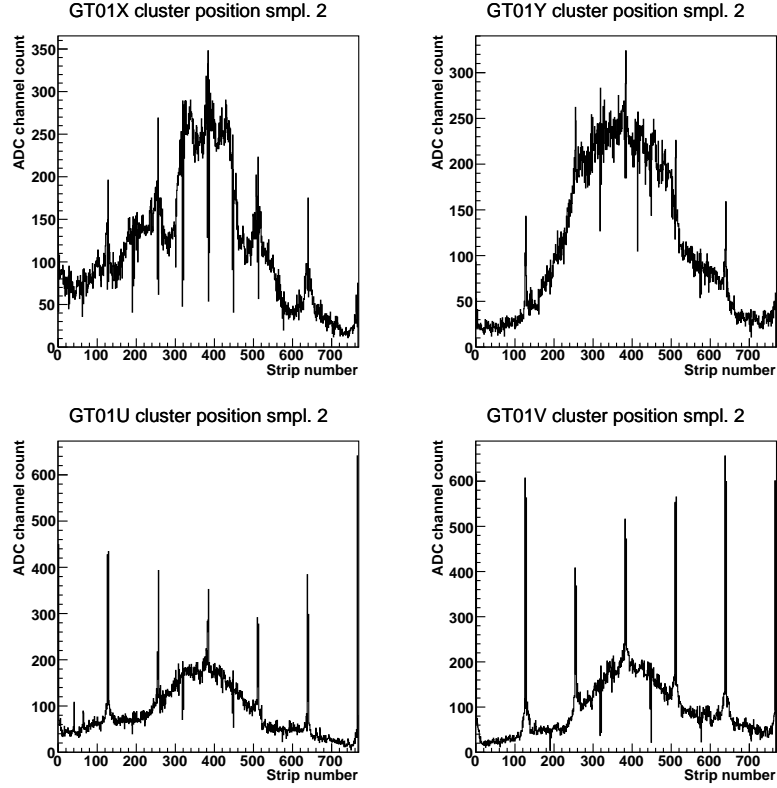


Fig. 36: Histograms which display the cluster charge in ADC channel counts vs. the cluster position in strip numbers for the corresponding projection.

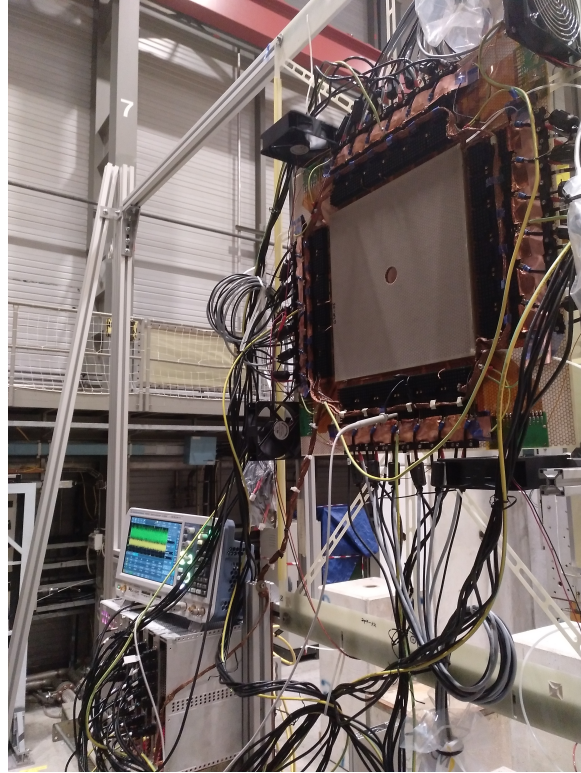


Fig. 37: Forth generation GEM detector prototype installed in the AMBER spectrometer for the 2023 PRM test run. A new third-generation GEM was fully instrumented with RD51 SRS-VMM electronics.

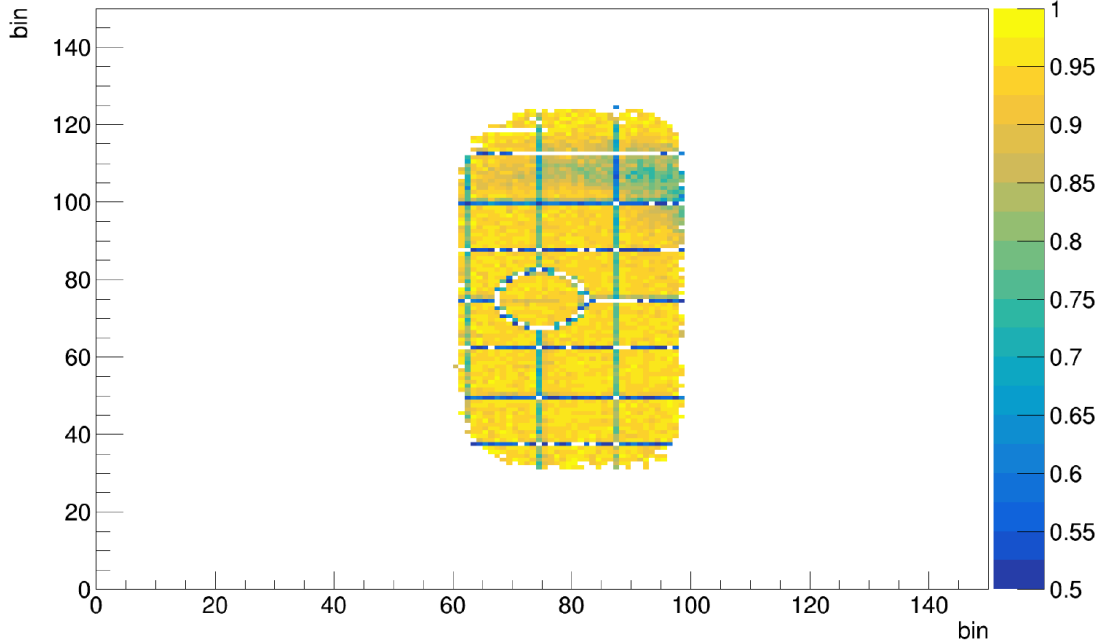


Fig. 38: Detector x-plane efficiency. The central detector part, where sufficient statistics due to the beam profile was collected. The circular, vertical and horizontal areas with lower efficiency coincide with the GEM sector gaps. The area with lower efficiency at the top right coincides with an area of lower GEM gain, for which the reason is currently under investigation.

## 6.7 Vertex Detector for Drell-Yan

As discussed in previous reports, to improve the mass and vertex reconstruction resolution for the AMBER's spectrometer for the Drell-Yan run, an active vertex detector is needed before the the hadron absorber to compensate for the energy loss and multiple scattering effect. A proposal was funded to reuse the sensors from the decommissioned Forward Silicon Vertex Tracker (FVTX) from the PHENIX experiment to build a silicon-strip vertex tracker (SVTX) for the AMBER experiment. The FVTX detector system is composed of two identical endcap sections located on either side of the collision point as shown in Fig. 39a. Each endcap has 4 layers of active silicon-strip sensors arranged in a disk around the beam pipe. The basic building unit is called a wedge, as shown in Fig. 39(c), which hosts two columns of the mini-strip silicon sensors and readout electronics. The mini-strips are aligned in the radial direction, with a pitch of  $75 \mu\text{m}$ , and cover  $7.5\text{deg}$  in  $\phi$ . A dedicated front-end ASIC, the FPHX chip, was designed to control and readout the silicon sensors. Each FPHX chip reads out 128 channels in a trigger-less data-push architecture and sends out the digitized time and amplitude information through extension cables to the upstream readout cards (ROC) which are located inside the interaction region (IR). The ROC boards combine and synchronize the data streams from up to 352 FPHX chips, and stream the data to the front-end module (FEM) located at the counting house via long optical fibers in a continuous and triggerless fashion. The FEM will sort and buffer the data from multiple beam crossings, and send out the event-of-interest once the level-1 trigger is received. The FEM also has an additional pair of optical fiber connections to the ROCs for slow control. The detailed specifications of the FVTX detector are summarized in Table 4.

The FVTX detector was designed and built by the Los Alamos National Laboratory (LANL) in collaboration with Fermilab and several PHENIX institutions. It was installed in PHENIX in 2012 and decommissioned in 2016 after PHENIX completed its last run. The ROC boards have been reused for the Intermediate Silicon Tracker (INTT) detector later sPHENIX experiment (2023 – 2025+), but the rest of the detector, including the sensors, front-end ASICs, mechanical supporting disks, and cooling system are still available. Due to the low radiation environment at PHENIX and short running time, the sensors have been only lightly used and are still fully functioning. We plan to reuse the FVTX sensors, front-end ASICs, and supporting mechanical structures to build a similar vertex tracker for the AMBER experiment.

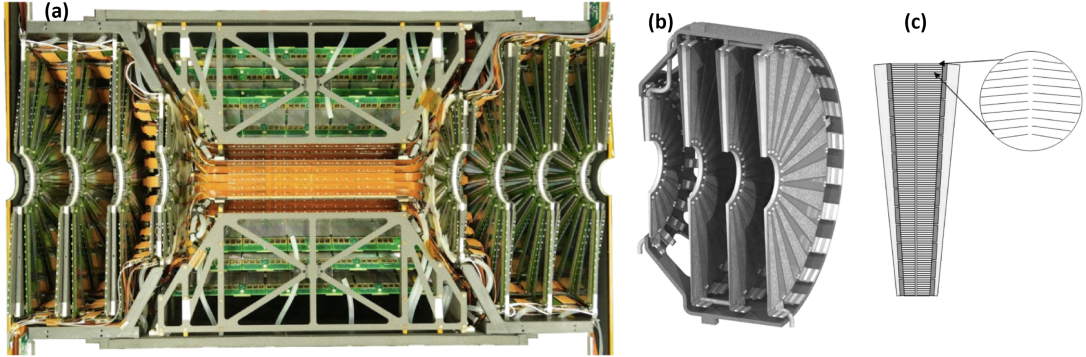


Fig. 39: (a) A completed half FVTX detector, with sensors, frontend electronics, supporting structures, and cooling system. Two half FVTX endcaps are shown on either end. The overall length is about 80 cm. (b) A structural illustration of one endcap of the FVTX. One small disk and three large disks are included in one endcap. (c) A segment (wedge) of the FVTX sensor. Each wedge holds two columns of silicon strips as shown in the zoomed-in portion.

Silicon sensor thickness ( $\mu\text{m}$ )	320
Strip pitch ( $\mu\text{m}$ )	75
Number of strips per column	1664
Inner radius of silicon (mm)	44
Outer radius of silicon (mm)	168.8
Strip length at inner radius (mm)	3.4
Strip length at outer radius (mm)	11.5
Pulse timing (ns)	30
Number of wedges per disk	48

Table 4: Summary of the FVTX specifications.



Fig. 40: Conceptual design of the silicon strip vertex detector placed downstream of the target stations. The silver and three blue cylinders show the upstream tungsten target and three carbon target stations. The orange disks show the placement of the large FVTX disks.

Fig. 40 shows a preliminary conceptual design where four large FVTX disks are placed between the third carbon target cell and the hadron absorber. Note upstream of the carbon targets there is a very thin (2 cm) tungsten target which is intended for additional nuclear dependence physics. The detector disks are placed very close to the third carbon target to maximize the detector acceptance and minimize the hit multiplicity and radiation dose. Four disks are used so that a local tracklet could be constructed with additional redundancy. To maximize the detector's  $\phi$  resolution, each of the four disks is shifted in  $\phi$  by  $7.5\text{deg}/8$  with respect to the neighboring disk. This conceptual design is incorporated into AMBER's GEANT4-based simulation software to study the expected performance.

Preliminary Monte-Carlo (MC) studies indicate that significant improvement in both vertex and mass resolu-

tion can be achieved with the current conceptual design, as shown in Fig. 41. Fig. 41(a) illustrates the vertex reconstruction of the DY MC events with the proposed vertex detector and compares it to the vertex distribution from MC truth and reconstruction without the vertex detector. It can be clearly seen that the vertex resolution is improved by roughly a factor of 4 with the SVTX. The much-improved vertex reconstruction can cleanly separate the muon tracks from different target cells, which completely recovers the efficiency loss due to the target geometry requirement and significantly reduces the possibility of having two independent muons misidentified as a dimuon. Fig. 41(b) shows the expected dimuon invariant mass spectrum from the simulated  $\pi$ -C data of two years of data taking with the proposed vertex detector, where significant improvement of the mass resolution of  $J/\psi$  and  $\psi(2S)$  resonances can be observed. In addition to mass and vertex, the reconstruction of other kinematic variables also benefits from the improved resolution brought by the proposed SVTX.

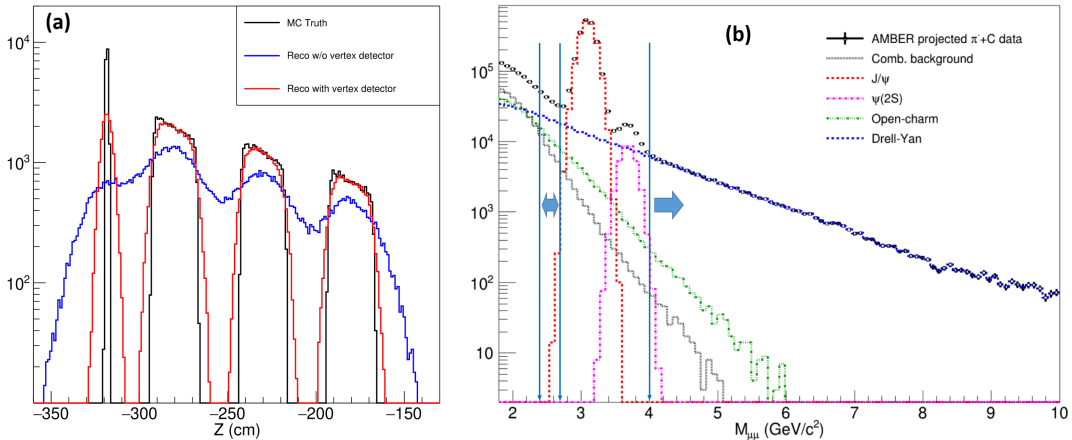


Fig. 41: (a) Vertex reconstruction of the dimuon MC data without the proposed vertex detectors (blue) and with the vertex detectors (red) compared with the generated vertex distribution (black). (b) MC simulation of projected dimuon mass spectrum from the  $\pi$ -+C data with the proposed SVTX after two years of data taking. The blue arrows indicate the mass range for the low- and high-mass DY events.

The project has been fully funded and started in late 2023. At this time, we are building a prototype telescope-like detector with the goal of including this detector at the Drell-Yan pilot run after the PRM data-taking before the LS3. Commissioning and operating the prototype detector during the first pilot run will enable us to validate the readout system design and the MC simulation for the detector performance. Upon completion of the pilot run, we will proceed with the full detector construction, which will entail a detailed sensor performance benchmark, refurbishment of FVTX's mechanical and cooling system, development of the high-level trigger and the online software, and procurement of the new ROC boards for the full detector. The full detector is expected to participate the two-year production run of the Drell-Yan program after the LS3.

## 6.8 FriDAQ

In 2023, the first test of the AMBER streaming DAQ with a real detector was performed. The results of this test are summarized above in (c.f. Sec. 4.2).

The current FriDAQ system is depicted in Figure 42 and includes the following components:

- DHMUX L0 FPGA modules to read detectors, which provide temporal information only. The L0 multiplexers are part of detector groups' responsibilities and are shown as an example;
- eight DHMUX L1 FPGA modules;
- one DHMUX Time Slice Builder;
- four ReadOut Engine Servers, each server equipped with PCIe card and 0.5 PByte external disk storage;
- High-Performance Ethernet switch and 100 Gbps link to the CERN Data Center;

- 100 Gbps link to CERN data center;
- HLT executed on HTCondor servers and reducing data by a factor 100;

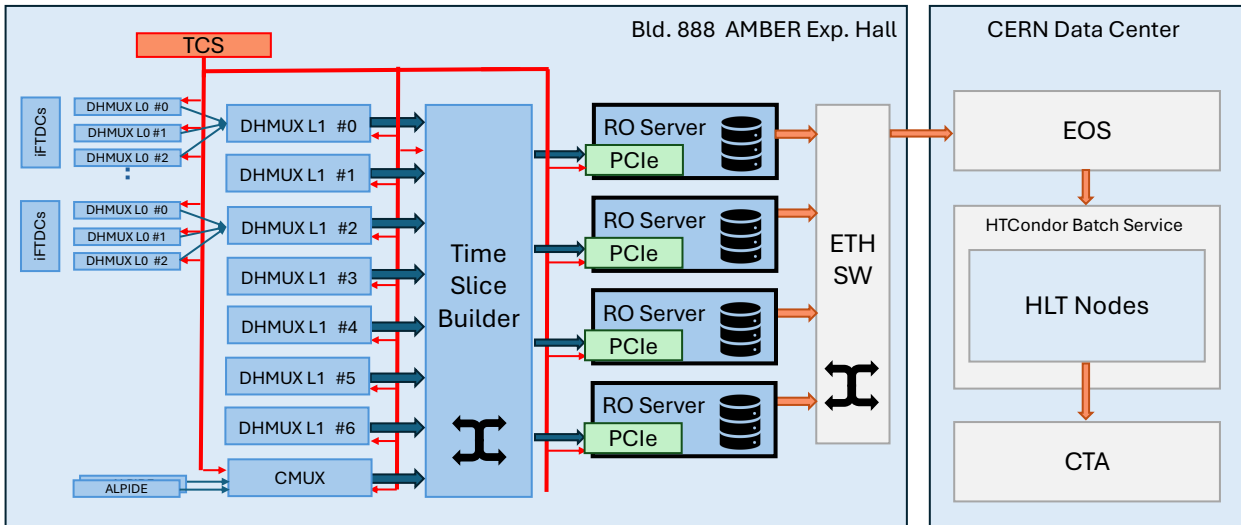


Fig. 42: A complete FriDAQ architecture for the PRM physics run including eight DHMUX L1 modules, one Time Slice Builder, and four Read-Out Engine servers equipped with 0.5 PByte disk space each.

This year we have started firmware development for DHMUX L1 multiplexer. The multiplexer plays a key role in the Time Slice Building algorithm by reducing the number of data links, equalizing the use of serial links to a level close to their maximum bandwidth, and providing data buffering for efficient operation of the Time Slice Builder. This development could not be started earlier due to limited manpower. The firmware reuses existing IP cores such as the TCS interface, IPBus protocol for configuration and monitoring, Aurora serial interface, and DDR3 interfaces. The integration of DHMUX L1 will be done in September alone with the upgraded version of DHMUX L0 firmware.

In 2024, we completed the purchase of DAQ computers and hardware components needed for the PRM physics run. The long-term performance of the DAQ chain was tested by transferring simulated data through local disk storage, to HLT servers, and finally to CTA. For the tests, the HLT emulated a CPU load of expected HLT algorithms. During the test, system performance scaled linearly with the number of the Read-Out Engines reaching a sustained data rate of approximately 4 GB per second.

## 6.9 Detector Control System

The Detector Control System (DCS) was updated according to the needs of the data taking for antiproton production cross-section measurements, mainly with the integration of the Liquid Hydrogen/Deuterium target described in subsection 5.1.

Information from the safety PLC system developed by EP-DT-DI was subscribed via DIP protocol and integrated into DCS. Visual and audible notifications were set up in DCS to help shift crews react in case of issues as well as email and SMS notifications for experts.

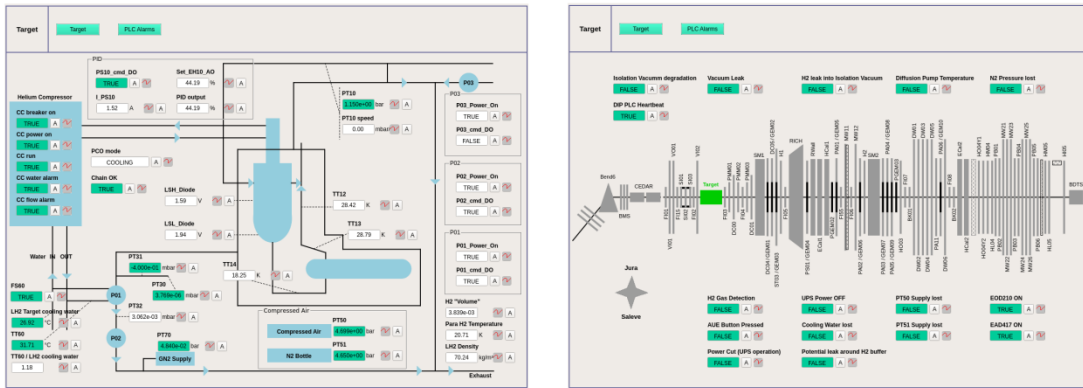


Fig. 43: AMBER DCS: Liquid Hydrogen/Deuterium target section.

Due to the fact that Atlas OpcUaIpBusServer had already been deprecated for some time, a new IPbus server for DCS was developed using the CERN DIM protocol. Monitored parameters from CEDARs IFTDCs, UCF multiplexers, Artificial Spill Structure Generator, etc were all moved to the new DIM server without any issue.

## 7 Publications, presentations to conferences and collaboration matters

In the past year, the AMBER Collaboration continued on establishing a protocol for managing its public dissemination and presentation endeavors. This was done by Publication Committee (PubCom), charged with responsibilities of coordinating and monitoring the internal approval process of all AMBER publications, as well as managing the acquisition, distribution, and assignment of talks and presentations throughout the scientific collaboration.

The central objective of the PubCom is to uphold the utmost standards for the public release of various types of AMBER results, encompassing oral presentations, posters, conference proceedings, electronic archives, and journal articles. The AMBER PubCom comprises four members, appointed by the AMBER Collaboration Board (CB) and serving terms of two years. These members are strategically selected to encompass the entirety of the collaboration's scientific endeavors, including the second phase of the experiment. The AMBER Analysis Coordinator is PubCom ex-officio member.

During 2024 the PubCom worked on the formulation of a set of regulations to govern the approval process for AMBER's physics results. A document outlining the procedures for pre-release, release and post release activities, for paper writing and submission, and for preparation of conference proceedings and other papers has been prepared and presented to AMBER CB and approved on June 27th 2024.

The PubCom is also directing its efforts towards contributions to conferences. Serving as a liaison, the PubCom offers a singular point of contact for conference organisers partnering with AMBER. This ensures AMBER's active visibility within the physics community, manifested through prominent participation in pertinent conferences, workshops, and educational events. Regular updates on upcoming conferences are managed by the PubCom and internally publicised within the collaboration. Additionally, the PubCom operates transparently, guaranteeing equitable distribution of presentations among AMBER collaborators, and extends editorial assistance for proceedings conducted on AMBER's behalf.

### Presentation to Conferences:

- 18 presentations to Conferences and Workshops in a period from August 1st 2023 to August 20th 2024.

## 8 References

### References

- [1] J. M. Friedrich and O. Denisov. AMBER Status Report 2022. Technical report, CERN, Geneva, (2022). URL <https://cds.cern.ch/record/2810822>.
- [2] J. M. Friedrich and O. Denisov. AMBER Status Report 2023. Technical report, CERN, Geneva, (2023). URL <https://cds.cern.ch/record/2868403>.
- [3] Aduszkiewicz et al., Measurements of  $\pi^\pm$ ,  $k^\pm$ , p and  $\bar{p}$  spectra in proton-proton interactions at 20, 31, 40, 80 and 158 GeV/c with the NA61/SHINE spectrometer at the CERN SPS, *The European Physical Journal C* **77** (2017) 671. ISSN 1434-6052. [doi:10.1140/epjc/s10052-017-5260-4]. URL <https://doi.org/10.1140/epjc/s10052-017-5260-4>.
- [4] H. G. Fischer for the NA49 Collaboration, Baryon yields, isospin effects and strangeness production in elementary hadronic interactions, *Acta Physica Hungarica Series A, Heavy Ion Physics* **17** (2003) 369–386. ISSN 1588-2675. [doi:10.1556/APH.17.2003.2-4.20]. URL <https://doi.org/10.1556/APH.17.2003.2-4.20>.
- [5] M. W. Winkler, Cosmic ray antiprotons at high energies, *Journal of Cosmology and Astroparticle Physics* **2017** (2017) 048–048. ISSN 1475-7516. [doi:10.1088/1475-7516/2017/02/048]. URL <http://dx.doi.org/10.1088/1475-7516/2017/02/048>.
- [6] M. Korsmeier, F. Donato, and M. Di Mauro, Production cross sections of cosmic antiprotons in the light of new data from the NA61 and LHCb experiments, *Phys. Rev. D* **97** (2018) 103019. [doi:10.1103/PhysRevD.97.103019].
- [7] M. Hoffmann. *PhD thesis in preparation*. PhD thesis, University of Bonn, HISKP, (2024).
- [8] A. Dziuba and A. Arutunova. private communication, (2024).
- [9] P. Abbon et al., The compass setup for physics with hadron beams, *Nuclear Instruments and Methods in Physics Research Section A: Accelerators, Spectrometers, Detectors and Associated Equipment* **779** (2015) 69–115. ISSN 0168-9002. [doi:<https://doi.org/10.1016/j.nima.2015.01.035>]. URL <https://www.sciencedirect.com/science/article/pii/S0168900215000662>.
- [10] K. Sidorowski. 169th EATM - XCED YETS 2023/24 Recap. Technical report, CERN, Geneva, (2024). URL [https://indico.cern.ch/event/1409983/contributions/5926578/attachments/2860184/5003961/169th%20EATM\\_XCED%20-%20YETS%202023-2024%20Recap.pdf](https://indico.cern.ch/event/1409983/contributions/5926578/attachments/2860184/5003961/169th%20EATM_XCED%20-%20YETS%202023-2024%20Recap.pdf).
- [11] K. Eichhorn. *PhD thesis in preparation*. PhD thesis, Technische Universität München, (2024).
- [12] M. Lupberger, L. Bartels, F. Brunbauer, M. Guth, S. Martoiu, H. Müller, E. Oliveri, D. Pfeiffer, L. Ropelewski, A. Rusu, and P. Thuiner, Implementation of the VMM ASIC in the Scalable Readout System, *Nucl. Instrum. and Meth. A* **903** (2018) 91–98. ISSN 0168-9002. [doi:<https://doi.org/10.1016/j.nima.2018.06.046>].